Chapter

Experimental Analysis of Waverider Lift-to-Drag Ratio Measurements in Rarefied and Supersonic Regime

Noubel Hugo and Viviana Lago

Abstract

This work, performed in the MARHY rarefied hypersonic facility, experimentally explores the effects of rarefaction on a classical waverider geometry. This hypersonic vehicle is designed to develop a shock attached along the leading edge length to improve flight efficiency. The concept was first proposed by Nonweiler in 1959. Since then, many studies have been conducted, mainly on numerical aspects. Few works have included the influence of the viscous effect, we can cite those of Bowcutt who showed how viscous effects impact the optimal shapes due to the skin friction drag. However, the trajectories of these types of vehicles anticipate flights with high Mach numbers and at high altitudes where rarefaction effects can strongly impact the lift-to-drag ratio predictions. This work focuses on the behavior of the L/D ratio at different supersonic operating conditions. The viscous effects were analyzed with 4 operating flow conditions: Mach 2 and 8 Pa static pressure and Mach 4 with 2, 8 and 71 Pa static pressures. For this purpose, the aerodynamic coefficients were measured for several angles of incidence. with a homemade sting balance. The experimental results were compared to Monte Carlo numerical simulations performed with the DS3V code.

Keywords: Waverider, Supersonic rarefied regime, Wind tunnel, Lift-to-Drag ratio, Sting balance, DSMC

1. Introduction

The classic hypersonic waverider is a vehicle geometry designed to capture the post-shock flow field between the waverider body, optimized at a specific Mach number and the flow. This specific geometry produces a high pressure region at the bottom surface of the vehicle that maximizes the lift-to-drag ratio (L/D). In general, hypersonic glider is designed to operate at Mach numbers higher than 5. This particular class of vehicle provides a higher L/D ratio than a generic vehicle for the same angle of incidence. However, the real advantage of hypersonic gliders lies in the fact that, for the same lift, the angle of incidence of the glider is much lower, which implies a low pressure drag compared to the generic vehicle. A very large number of geometrical configurations of hypersonic gliders have been developed since the late 1950s. One can refer to the recent review article published by Ding

et al. [1] which gives an overview of the different hypersonic glider geometries published to date. However, the usual methodology to create a hypersonic glider geometry remains the same as it is based on the generation of a shock from a canonical geometry: cone, von Karman warhead, wedge, etc. Depending on the desired characteristics (Mach, altitude, angle of incidence, etc.), the shape of the hypersonic glider is generated by projection onto the shape of the shock wave generated by the canonical shape. This implies that a hypersonic glider is only defined for a given operational configuration, nevertheless very recent works have generated geometries optimized for several Mach numbers and tested by numerical simulations (Mach 5 and 10) [2].

When a hypersonic glider evolves at high altitude in a rarefied flow, additional flow characteristics must be taken into account for the design of glider geometries. Indeed, viscous effects appear, it is possible to take them into account in the initial definition of the geometry [3, 4]. In particular, the process of viscous interactions (strong and/or weak) will generate a modification of the shape of the shock waves: in the case of a strong interaction, the boundary layer that develops will "push" the shock outwards. The fluid layer between the shock and the boundary layer will then act on the development of the boundary layer, thus setting up a phenomenon of mutual interactions [5]. In addition, as the flow becomes thinner, especially near the leading edges, the shock waves become more and more detached from the geometry, leading to interactions between the lower and upper parts of the glider on both sides. This results in a significant decrease in lift due to the "emptying" (spillage) of the high pressures initially located under the glider and which are the origin of the lift effect sought for hypersonic gliders. Moreover, the progressive development of viscous drag, especially on the upper part of the geometry, inevitably leads to an increase in the overall drag [6]. The combination of these two effects leads to a strong decrease of the L/D ratio, thus strongly degrading the aerodynamic performance of hypersonic gliders. These effects have been demonstrated by numerical simulations but, to date, there are no experimental results in the literature that have demonstrated and quantified them.

It can also be noted that for Mach numbers of about 15, rarefaction effects can begin to appear from 40 km altitude. As a reminder, it is generally considered that we are in the presence of a rarefaction flow for altitudes above 60 km. This result was indirectly confirmed by Rault [7] who showed, via numerical simulations, that the flow in the vicinity of a hypersonic glider was mainly in rarefaction regime whereas the Knudsen number calculated with infinite flow conditions indicated rather that the flow was in continuous regime. Thus, rarefaction effects may be present at a much lower altitude than expected.

To take into account these rarefaction effects, a new category of hypersonic gliders was created in the 1980s with the pioneering work of Professor Anderson of the University of Maryland [8–10], introducing the "viscous optimized waveriders". Currently, most of this type of waverider is studied in China, in particular Liu et al. [11] shows that the considered altitude (thus the level of rarefaction) influences significantly the shape of the gliders, playing notably on the volume of the payload.

Regardind the identification of rarefaction effects and their quantification, to our knowledge only results from numerical simulations exist [12–14]. Experimental results from wind tunnel tests are currently absent from the literature. Indeed, a quick overview of the experimental work undertaken on hypersonic gliders shows the lack of experimental data concerning rarefied flows in the slip or transition regime. This is explained by the lack of experimental facilities to simulate this flow regime at high Mach number, but also by the metrological difficulties inherent in the characterization of rarefied flows. Concerning hypersonic gliders, the studies

presented in the literature only concern medium altitudes: 22.5 km [15] or 30.6 km [16]. The very few studies conducted in the rarefied regime [17–19], contain only fragmentary results which do not allow to highlight the effects of rarefaction on the aerodynamic performance of hypersonic gliders, and even less to quantify them over a wide range of flow conditions.

To overcome the lack of experimental data available in the literature, correlation functions are often used to extrapolate the aerodynamic behavior of these types of vehicles at high altitude. These correlations are based on old experimental data or are relative to canonical (thus simplified) geometries [20].

Moreover, these semi-empirical laws often use parameters based on quantities that must be measured locally, such as pressure or wall temperature [21]. Thus, the use of existing bridging functions can lead to an approximate evaluation of the aerodynamic coefficients of hypersonic gliders, especially since the diversity of existing geometries is large. It is therefore necessary to establish empirical correlations suitable for hypersonic gliders in rarefied flow at high Mach number.

By exploring a field that is currently poorly studied experimentally, the knowledge acquired on rarefied hypersonic flows around complex 3D geometries will be directly useful to actors planning the development of new atmospheric re-entry vehicles, such as space agencies and aerospace industries. In particular, the hypersonic glider concept is also being considered as an atmospheric re-entry or planetary transfer vehicle: [22, 23] for space exploration of telluric planets, gas giants, or some of their moons, for which trajectory control is also central to the success of a space exploration mission [24].

The main objective of this study is to determine experimentally if rarefaction effects significantly modify or not the aerodynamics of hypersonic gliders when they fly at high altitude in rarefied atmosphere. This study will be carried out with the MARHy rarefied hypersonic wind tunnel of the FAST experimental platform of the ICARE laboratory, which allows to cover the flight conditions in terms of Reynolds/Mach of glider trajectories for altitudes ranging from 100 km to 60 km. This paper focuses on measurements of the aerodynamic forces of a classical hypersonic glider in Mach 4 and Mach 2 flows with different Knudsen numbers in order to study the correlations between viscous effects and L/D ratios.

2. The model definition

2.1 General waverider concepts

Lifting vehicles founded a real interest since the late 1960s, in USA with the development of the Space Shuttle orbiter design based on a flat delta plate shape. In the same time, much works originated from Europe focused on more generalized research which differ from the pattern of American research. In particular, European effort concerned the aerodynamics of lifting reentry in hypersonic regime with the design and performance of so called waveriders [25]. The concept of waverider was introduced in 1959 by Nonweiler [26] as a type of delta wing and was named caret waverider. During its works, Nonweiler noted that the shock create a high pressure on intrados (the under surface) and induced lift. The main concept to design a waverider can be summarized by the idea that the lower surface is generated from the streamlines of the flow over a body and the upper surface is aligned with the free stream flow. During the early 1980s, waveriders design have been improved thanks to Rasmussen studies [27]. Rasmussen used the shock created by the flowfield in contact with a canonical geometry to generate lift. This method allowed to obtain waveriders with better performances than Nonweiler's design.

Based on Ramussen method other studies were carried out to optimize the geometry and increase the Lift-to-Drag ratio, giving birth to various families of cone derived geometries as well as hybrid variations like cone-wedge waveriders [28, 29]. Waveriders are designed to maximize lift-to-drag for a flight specific conditions (Mach, altitude). Nevertheless during the flight, altitude and speed will change getting out of their optimized flight domain range leading to uncertainties regarding their aerodynamic behavior [30, 31].

2.2 The experimental waverider definition

This experimental work intends to study the influence of rarefaction effects on the aerodynamic performances of the waverider (lift, drag and L/D ratio). To do so, we have looked for an optimal geometry close to our experimental test conditions in rarefied regime. The geometry we have designed is based on the Rolim geometry which is optimized for an altitude between 40 km and 50 km and a speed of Mach 10. This geometry, if not optimal, has been optimized for altitudes close to the one simulated in our wind tunnel between 50 km and 80 km. Concerning the Mach number, the experimental tests have been carried out at Mach 2 and Mach 4, far from the Mach 10 conditions proposed by Rolim. This Mach number discrepancy allowed to study the aerodynamic behavior of the waverider for speeds lower than the expected one as well as its evolution outside its privileged flight domain. The waverider is 100 mm long, 35.7 mm wide, 6.6 mm high, **Figure 1**, and the dihedral angle,Φ, is approximately 53°, and it was 3D printed in resin. The dimensions of the waverider were chosen according to the test area of the wind tunnel.

3. Aerodynamic forces measurements

3.1 The sting balance description

An aerodynamic balance has been developed to measure drag and lift forces in the MARHy operating flow conditions. The main difficulty comes from the fact that operating conditions concerns rarefied regime with low density flows, giving force values estimated between 1mN and 1 N. Aerodynamic balances applied to supersonic wind tunnels are ranged in two main balance groups' internal and external balances. Internal balances [32] are a test model extension and located inside the test section, on the contrary, external [33] are placed outside the test section and the model is supported with thin wires. For the present study, a sting balance was designed to measure drag and lift forces applied to the waveriders in supersonic and hypersonic flows. The design of this device had to meet to several constraints: be able to measure small forces values around mN, to have an aerodynamic design to not obstruct the test section and ability to measure aerodynamic model forces with different incidence angles without changing the balance calibration. This sting balance is composed in two parts, drag and lift modules as showed on **Figure 2**. The principle adopted for force measurement is based on the deformation of thin slats equipped with strain gauges, deforming when the test model is an incoming flow.

The drag module as can be seen on **Figure 3** is designed in three parts: upper part, slats, and lower part in order to facilitate manufacturing. There are six slats arranged in three rows and two columns. Indeed, many configurations have been dynamically simulated with a CAO software to optimized de number of lamelles, their arrangement and their thickness. The **Figure 3** shows the deformation of the drag module slats when subjected to a horizontal force. The results showed that this configuration is the best compromise to optimize the bending, and to minimize the

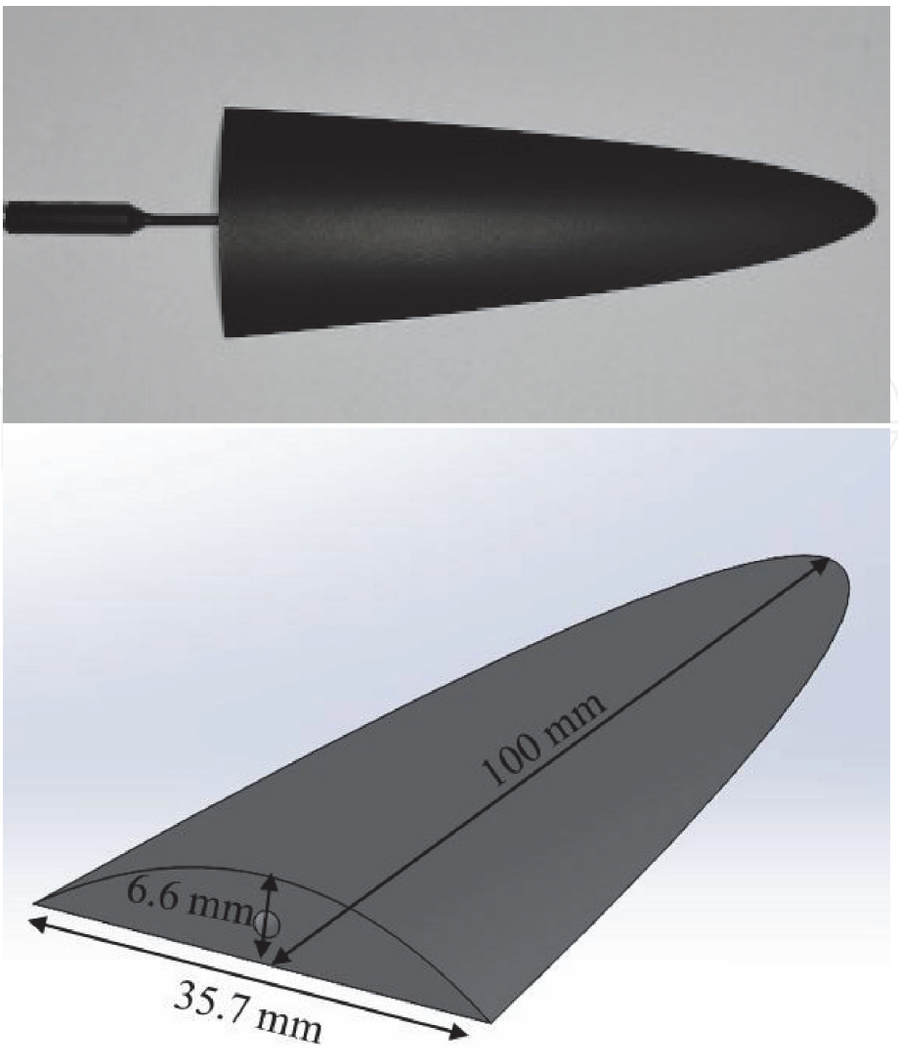

Figure 1.
3D CAO design of the waverider used in this experimental work.

Figure 2.
View of the sting balance two modules, drag and lift.

lateral and vertical deformations. Indeed, other configurations such as a row of three wider slats showed lateral and vertical deformations that could weaken the balance of the sting, optimizing the bending which is the most important part for this module.

The drag slats are 0.2 mm thick and made of AISI 304 steel to avoid plastic deformation. Once all the components of the drag module are assembled, the lower

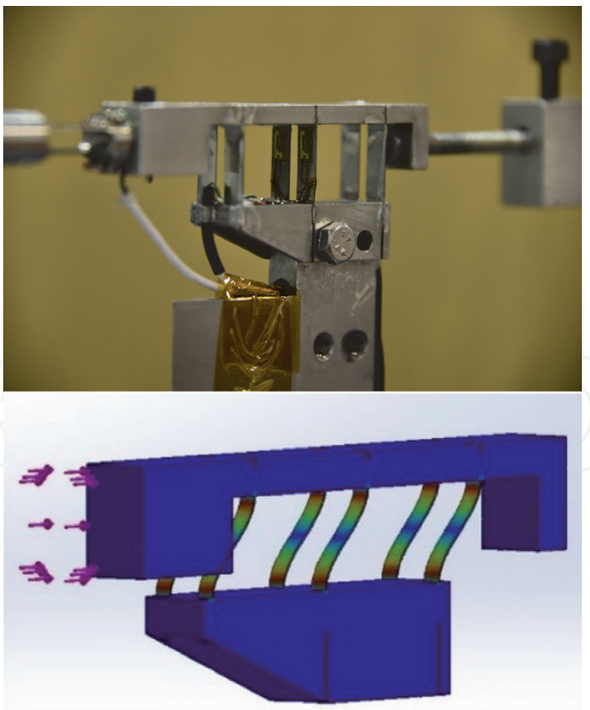

Figure 3.
Detail of the drag module and simulation of the strain stresses.

part is static and only the upper part is mobile. Therefore, the most sensitive part of the slats is the upper area, where the strain gauges will be placed. The strain gauges are glued to the central slat and there is one on each side to create a complete Wheatstone bridge. The lifting module is made up of a single part and there are only two superimposed slats. This module is also made of AISI 304 and it measures 10 cm. The purpose of having two superimposed slats is to reduce the bending of the heavy test models when the flow is deactivated. Indeed, if the test model creates a bending due to its mass, it can have an impact on the lift values in the presence of the flow. The maximum mass of the test model that this sting balance can support is 140 g. This lift module, like the drag module, has a full Wheatstone bridge with two strain gauges per side, as shown in **Figure 4**.

Drag module measurements are dependent on the position of the balance center of gravity (COG). A change in the position of the center of gravity will change the measurement of the associated forces for the same test model and flow conditions. To avoid this problem, a counterweight is placed at the back of the balance and its position is adapted according to the mass of the test model. The higher the mass of the test model, the further the counterweight will be from the drag module. On the contrary, if the test model is light, the counterweight will be closer so that the center of gravity is always aligned with the two slats equipped with strain gauges.

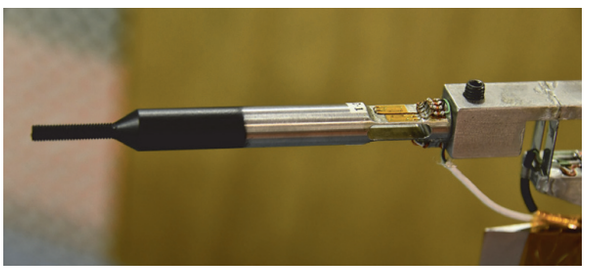

Figure 4.
Detail of strain gauges of the lift module.

Another important point for this type sting balance is to avoid that the flow has a direct impact on the deformation of the slats. Indeed, if the drag and lift modules are in the flow without protection, the drag and lift values will be overestimated. In addition to the shock produced by the presence of the test model, a second shock can be created on the drag module itself and increase the deformation of the slats and thus the drag value. To solve this problem, a cover was modeled and installed. It is dimensioned to allow the drag and lift modules to deform without touching the cover which could create friction and in turn distort the measurements. On the other hand, this cover also allows to protect the strain gauges from the temperature increase caused by the shock in hypersonic flow condition. For the experimental conditions of this work in supersonic regime, the shock does not produce any heating.

To validate this sting balance, we have performed a study with spheres in order to compare our experimental results with those of the literature. In his study, Aroesty determines the drag coefficients for spheres in a supersonic flow at Mach 4 and low density and establishes a curve that relates the drag coefficients of the spheres with the Reynolds number after shock Re2 [34]. In our case we measured the drag forces for spheres of different diameters in the three flow conditions at Mach 4. **Figure 5** plots the experimental data from Aroesti and our experimental results. As shown in the graph, the drag coefficients for the sting balance are consistent with the reference values. The numerous preliminary tests we have conducted have shown that without the stinger cover, the drag coefficients for small diameter spheres (less than 15 mm) and low Re2 (less than 200) are indeed overestimated as explained in the previous paragraph. For larger diameter spheres, the results are close to the Aroesty values without the protective cover. This is due to the fact that the shock created by the large diameter spheres is large enough to protect the scale elements that will be in the wake, which is not the case for the small diameter spheres.

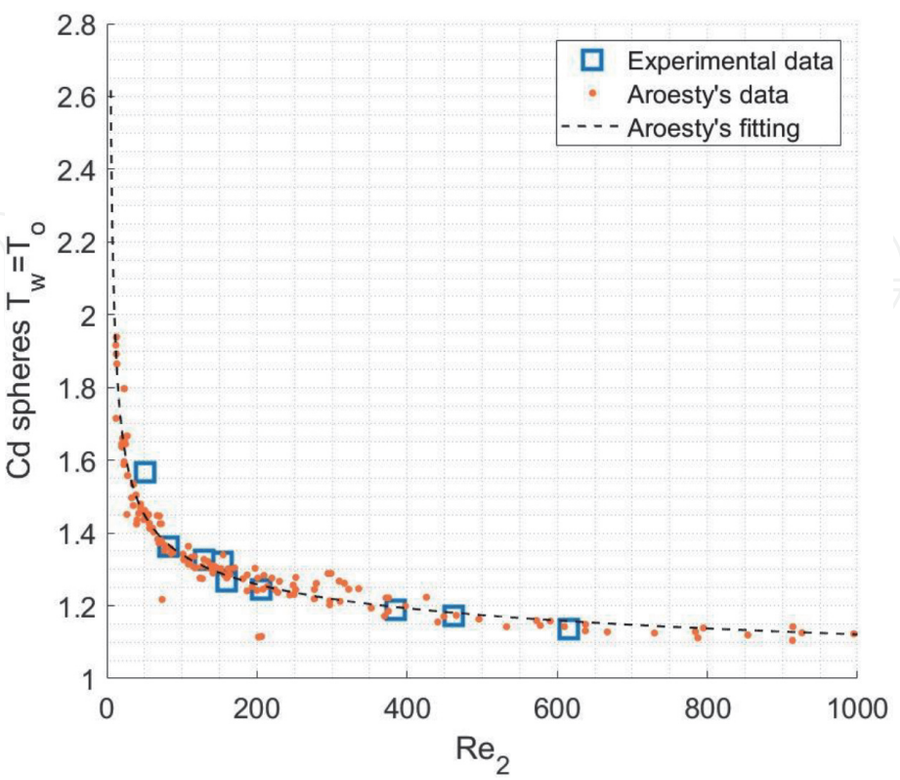

Figure 5.
Drag coefficients of spheres in near rarefied regime: Aroesty and Noubel data.

3.2 Strain gauges

Strain gauges are used to measure the slat deformation. It is a sensor whose resistance varies with the applied force, then it converts force into an electrical resistance which can then be measured [35]. Strain gauge elements are electrically connected to form a Wheatstone bridge circuit used for the measurement of static or dynamic electrical resistance. The output voltage of the Wheatstone bridge is expressed in millivolts output per volt input. At the end a calibration curve of the lift and drag modules will convert the out put signal in a mesure of the corresponding fonce expressed in newton. For the experimental conditions of the MARHy wind tunnel forces are estimated between 1 mN and 1 N so strain gauge need to have a high gauge factor. There are essentially two types of strain gauges, the so-called semiconductor strain gauges whose gauge factor is greater than 180 and the metallic strain gauges whose gauge factor is between 2 and 3. In order to optimize the measurement of forces we have opted for the first type, however they are very sensitive to the value of excitation applied which can easily damage them [36, 37]. For this balance, the gauge used is the KYUOWA: KSPB-2-1 K-E4, with an excitation voltage of 1 Volts.

3.3 Calibration procedure

Calibration of the balance is necessary to convert the electrical signal from by strain gauges into applied force. The purpose of calibration is to reproduce known forces on the sting balance and relate them to the variation of the measured voltage. We designed a calibration bench composed of a digital newton meter mounted on a motorized micrometric displacement, which aligned with the lift or drag modules, apply a stable and known force in the same geometric configuration as those of the experience. Both during calibration and during wind tunnel experiments, the models are screwed onto the model holding sting so as to align their center of gravity with the end of the sting. Finally a curve is obtained expressing the force as a function of the voltage measured for each module: drag and lift. The accuracy of the force measurement on the lift and drag module is estimated at 0.1 mN.

A counterweight is added so that the position of the center of gravity remains constant regardless of the size and mass of the model. This preserves the calibration performed with the balance provided that, during wind tunnel measurements, the balance's center of gravity is in the same position as during calibration. For this purpose, the position of the counterweight is adjusted for each test model.

It should be noted that if the aerodynamic forces are to be studied as a function of the angle of incidence of the test model with respect to the flow, it must be ensured that the center of gravity remains unchanged. For this reason, the balance is positioned horizontally so that the angle of incidence in the horizontal plane (x-y) is changed and the position of its center of gravity is not affected [38].

4. Experimental conditions

4.1 Marhy facility description

The first version of the wind tunnel, then named SR3, was built in 1961, at the Aerothermic Laboratory. Since 2000, this wind tunnel, renamed MARHy, has been installed at the ICARE Laboratory of the CNRS in Orléans, and many technical improvements have been made.

In particular the pumping unit which is a key element allowing to ensure in continuous mode without time limit low density flows with Mach numbers ranging

from 0.8 to 21. The two main components of the Marhy facility are the large capacity test chamber and the pumping unit. The wind tunnel consists of three main parts: the settling chamber, the test chamber and the collector-diffuser chamber as presented in **Figure 6**.

The facility is supplied with exchangeable nozzles to generate laminar subsonic, supersonic and hypersonic stationary flows [39]. Only the supersonic configuration is described in this paper.

Subsonic and supersonic conditions flows are generated by contoured nozzles, using air or nitrogen at ambient temperature. Nozzles are housed into the settling chamber, a cylinder of 2.6 m length and 1.2 m in diameter with a large access port at the bottom (200 *kg*), placed on a trolley with wheels on a guide rail for easy opening and closing. The relevant components of the facility MARHy in supersonic configuration is skecthed on **Figure** 7.

The divergent section of the nozzles opens into the experimental chamber, a cylindrical test section with a diameter of 2 m and a length of 3.5 m.

This chamber is placed perpendicular to the direction of the flow, so that there is enough space on either side of the flow to install diagnostic systems and supports without disturbing the flow. The experimental chamber is large enough to allow the

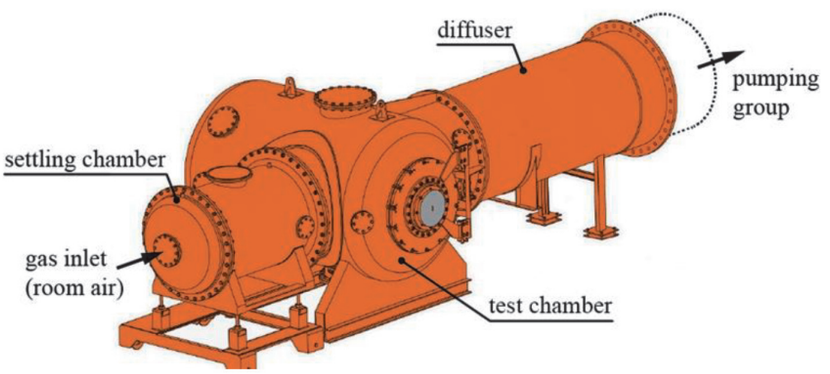

Figure 6.
The wind tunnel MARHy and the pumping group.

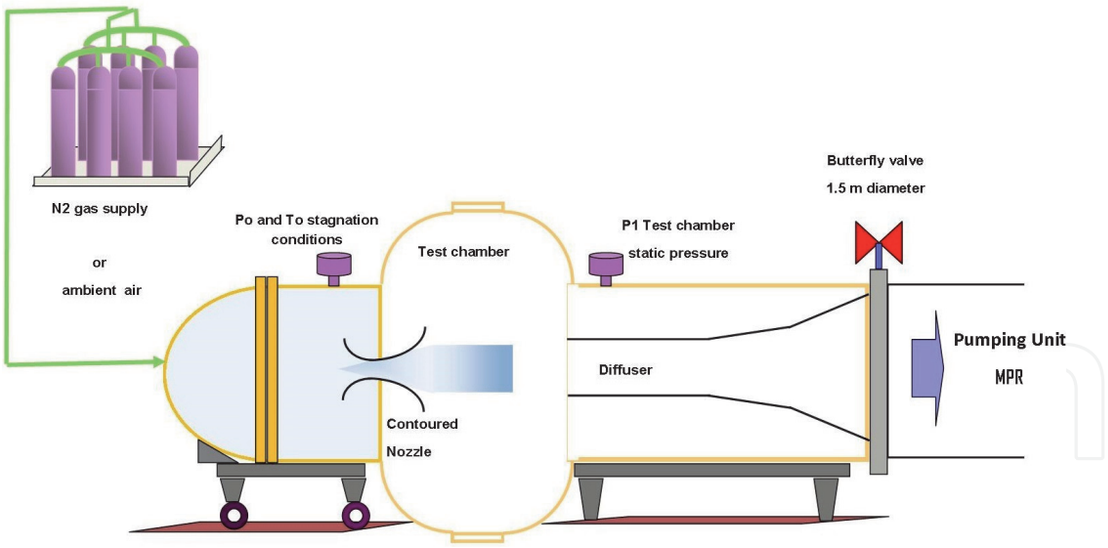

Figure 7.
Sketch of the wind tunnel MARHy in supersonic configuration.

integration of specific instrumentation such as probe supports, electron gun and aerodynamic balances and to avoid interactions between the flow and the wall of the wind tunnel. Two rounded bottoms laterally close the cylinder, one of them is provided with a door of 1.2 m in diameter, giving access to the interior of the experimental chamber as can be seen in **Figure 8**. Four port flanges with a diameter of 0.6 m, closed by optical windows made of quartz and fluorine, are distributed around its cylindrical section. Six other smaller diameter flanges are available for instrumentation.

The pressure in the experimental chamber is recovered by means of a central diffuser to match the test section pressure to the inlet pressure for the vacuum pumps, specially at hypersonic operating conditions. The collector-diffuser is a 1.4 m diameter cylinder connects the experimental chamber to the pumping group by means of a motorized butterfly valve with a diameter of 1.5 m. The pumping group consists of 2 primary pumps, 2 roots-type intermediate pumps and 12 roots-vacuum pumps,ensuring continuous operation. The number of pumps commissioned depends on the operating conditions of the flow (Mach number and static pressure).

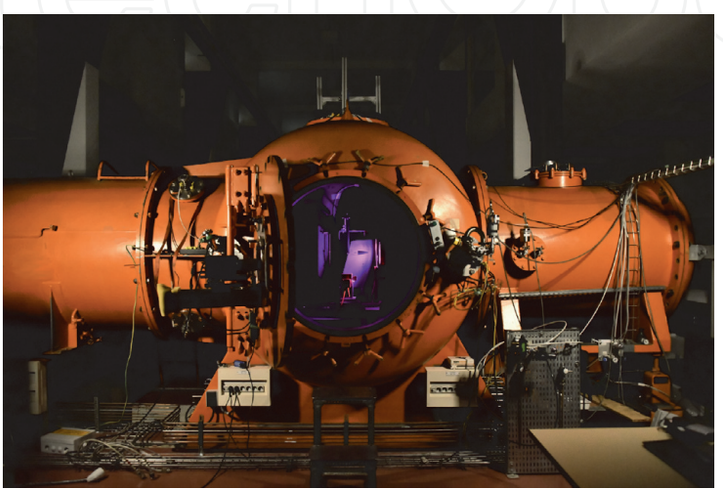

Figure 8.
View of the experimental chamber of the facility MARHy.

4.2 Operating conditions

One of the major advantage of the facility is its almost unlimited running time, particularly suitable to obtain a good stabilization of the flow conditions prior to experiments.

The purpose of this experimental study is to investigate the influence of rarefaction effects on the flight performance of waveriders with isobar and isomach operating conditions. Among the available nozzles we have selected four to carry out this first part of the study in supersonic conditions. The Isobar conditions are obtained with a static pressure of 8 Pa with the nozzle N1 operating at Mach 2 and nozzle N3 operating at Mach 4. Isomach conditions are performed at Mach 4 with the nozzle N2 operating with a static pressure of 2.66 Pa, the nozzle N3 with a static pressure of 8 Pa and the nozzle N4 operating with a static pressure of 71 Pa. The detailed operating conditions for these nozzles are presented in **Tables 1–4** where p represents the pressure, T the temperature, ρ the volumetric mass density, U the flow velocity, M the Mach number, λ the mean free path and R_e the Reynolds number based on the length L = 100 mm and calculated with the relation $R_e = U_1 L/\mu_1$, where μ_1 is the kinematic viscosity.

Various parameters have been proposed to quantify the rarefaction effects that make the Navier–Stokes equations invalid. The Knudsen number, defined as the ratio of the mean free path to a characteristic length, is a measure of the gas density

Stagnation conditions	**Free stream conditions**
$p_0 = 63$ Pa	$p_1 = 8$ Pa
$T_0 = 293$ K	$T_1 = 163$ K
ρ_0=7.44.10^{-4} kg.m^{-3}	ρ_1=1.71.10^{-4} kg.m^{-3}
	μ_1=1.10^{-5} Pa.s
	$U_1 = 511$ m.s^{-1}
	$M_1 = 2$
	$\lambda_1 = 0.278$ mm
	$R_e = 77.3$ /cm

Table 1.
N1 (Mach 2–8 Pa) operating conditions.

Stagnation conditions	**Free stream conditions**
$p_0 = 405$ Pa	$p_1 = 2.66$ Pa
$T_0 = 293$ K	$T_1 = 70$ K
ρ_0=4.81.10^{-3} kg.m^{-3}	ρ_1=1.33.10^{-4} kg.m^{-3}
	μ_1=4.77.10^{-6} Pa.s
	$U_1 = 670$ m.s^{-1}
	$M_1 = 4$
	$\lambda_1 = 0.219$ mm
	$R_e = 180.5$ /cm

Table 2.
N2 (Mach 4–2.66 Pa) operating conditions.

Stagnation conditions	Free stream conditions
$p_0 = 1214$ Pa	$p_1 = 8$ Pa
$T_0 = 293$ K	$T_1 = 70$ K
ρ_0=1.44.10^{-2} kg.m^{-3}	ρ_1=3.99.10^{-4} kg.m^{-3}
	μ_1=1.10^{-5} Pa.s
	$U_1 = 670$ m.s^{-1}
	$M_1 = 4$
	$\lambda_1 = 0.072$ mm
	$R_e = 541.5$ /cm

Table 3.
N3 (Mach 4–8 Pa) operating conditions.

Stagnation conditions	Free stream conditions
$p_0 = 10797$ Pa	$p_1 = 71$ Pa
$T_0 = 293$ K	$T_1 = 70$ K
ρ_0=0.13 kg.m^{-3}	ρ_1=3.55.10^{-3} kg.m^{-3}
	μ_1=4.77.10^{-6} Pa.s
	$U_1 = 670$ m.s^{-1}
	$M_1 = 4$
	$\lambda_1 = 0.008$ mm
	$R_e = 4806.7$ /cm

Table 4.
N4 (Mach 4–71 Pa) operating conditions.

and is in fact a state parameter. Other correlation parameters must be taken into account for rarefied high velocity flows as indicators of when the Knudsen number is not a flow parameter for supersonic flows in the sense that Mach number and Reynolds number are flow parameters. To account for viscous effects due to rarefaction and high velocity flow, the similarity number $\psi = \frac{M}{\sqrt{Re}}$, called the viscous parameter is a better candidate where the Reynolds number reflects the dynamical similarity of the flows around a model and the full-scale object [40–42]. It is important to note that in this investigation the wall temperature of the waverider remains "cold", with $T_{wall} = T_0$.

Table 5 sumarizes the values for the Knudsen number, the Reynods number, and the viscous parameter for each of the nozzles used for this investigation.

Parameter	Mach2-8 Pa	Mach4-2 Pa	Mach4-8 Pa	Mach4–71 Pa
Kn	2.78.10^{-3}	2.09.10^{-3}	7.33.10^{-4}	8.25.10^{-5}
Re	773.8	1805	5415	48067
Viscous parameter	0.227	0.0943	0.0544	0.0182
Re2	514.84	513.15	1539.46	13687.61

Table 5.
Nondimensional parameters for each one of the nozzles (based on L = 10 cm).

4.3 Measurements protocole

The supersonic nozzles of the wind tunnel are curved nozzles which will produce isentropic flows by adjusting the generating pressure P_o and the static pressure P_1 measured in the test section. The latter will be adjusted by adjusting the opening of the motorized butterfly valve which separates the test chamber from the pumping unit.

The test model is positioned in the isentropic zone, where the flow conditions are stabilized as showed on **Figure 9**. Outside this zone, the Mach number and pressure change and no longer correspond to the isentropic values for each nozzle. The total force measured by the balance corresponds to the force exerted by the flow as well as that created by the suction of the pumping unit. In order to keep only the force created by the flow, a measurement of the residual pumping force is made by isolating the model/balance assembly from the flow. To do this, a plate mounted on a rotating piston is inserted into the flow in front of the model, so that the model is no longer subject to the aerodynamic forces generated by the flow. The force of interest is the difference between the total force and the residual force.

The aerodynamic force measurements are done in two steps: first, the values of the drag and lift modules corresponding to the waverider exposed in the flow are recorded, then in a second step, the plate is placed between the waverider and the flow to record the offsets of both modules. For both steps, the acquisition time is 10 seconds with an acquisition frequency of 1000 kHz. This operation is repeated 5 times for each position of the wave rider in the flow, in order to have an average value which is representative of the aerodynamic forces. Since the isentropic flow is homogeneous in a given volume which depends on the nozzle used, special attention has been paid to the placement of the waverider in the flow whatever the angle of incidence. For this purpose, the position of the waverider is corrected using motorized translations, so as to reposition the waverider to its initial position without angle of incidence as illustrated on **Figure 10**. The reference point is the center

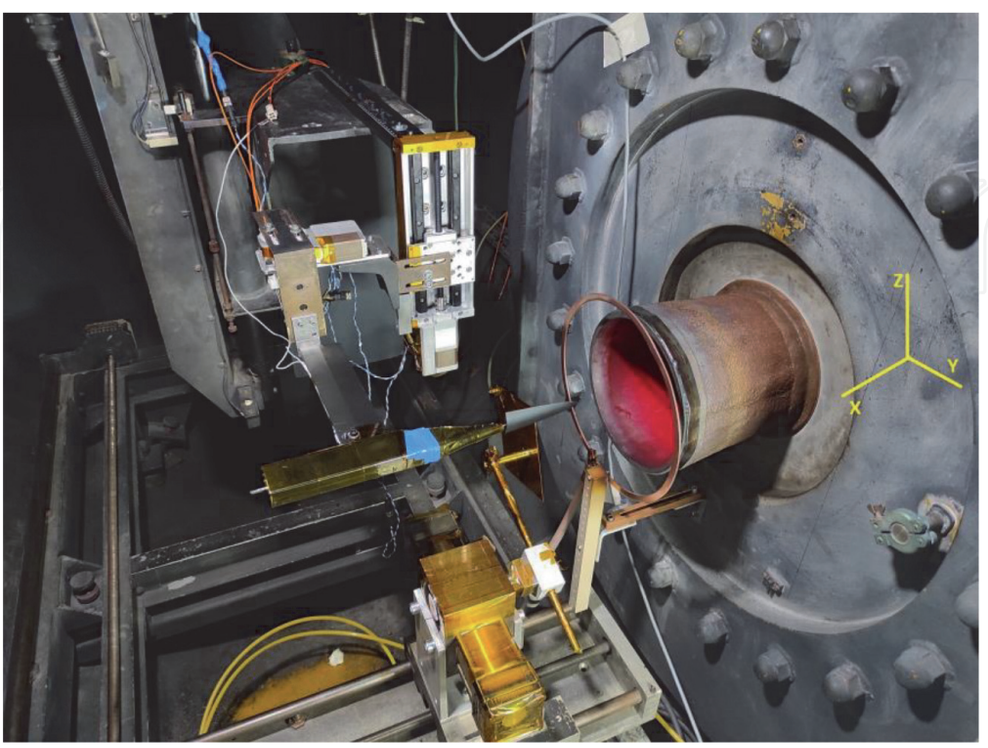

Figure 9.
Assembly of the sting balance/model in the test chamber.

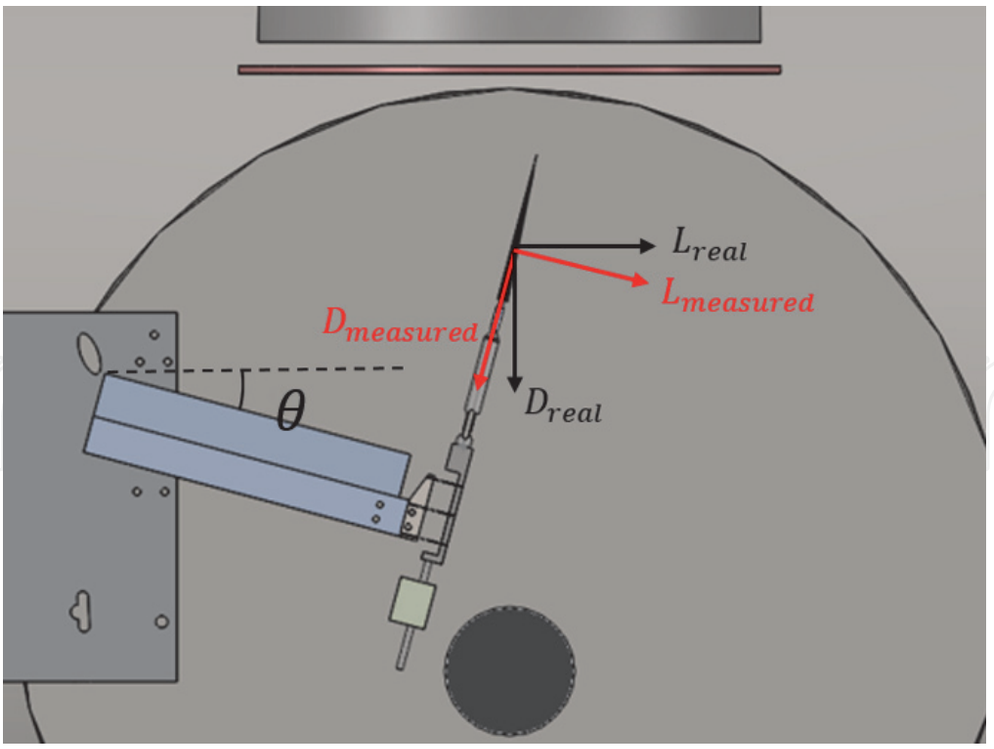

Figure 10.
Coordinates correction of the model location in (x-y) plane.

of the waverider. The determination of the drag and lift forces is a function of the measured values of the respective modules and the angle of attack of the waverider. The correction is given by changing the Cartesian coordinates into cylindrical coordinates following these equations:

$$Drag_{real} = Drag_{measured} * cos(\Theta) + Lift_{measured} * sin(\Theta) \quad (1)$$

$$Lift_{real} = Lift_{measured} * cos(\Theta) - Drag_{measured} * sin(\Theta) \quad (2)$$

5. Results

5.1 Measurements of lift and drag forces

The lift-to-drag ratio is of most important consideration when designing spacecraft and others space vehicles to reach higher lift-to-drag ratios. In addition to their shape, the incidence angle plays a significant role over the lift-to-drag ratio. The incidence angle is defined as the angle at which the leading edge of the vehicle is set in relation to the flowing air, and has a direct influence on how far the vehicle will glide for a given altitude. At high Mach numbers or high altitudes because of viscous effects, the skin friction will increase the viscous drag, decreasing L/D ratios.

Drag and lift forces have been measured for each one of the nozzles and for several angle of attack covering negative and positive angles. The objective is to study the behavior of the waverider in gliding phase, maximizing the Lift-to-Drag ratio (positive angles) and in the landing phase, reaching a target as quickly as possible (negative angles). For nozzles N1 and N2, the attack angles range between −25° and 25° while for N3 and N4 angles are ranged between −50° and 25°. It was not possible to achieve angles below −25° with nozzles N1 and N2 because the vacuum pumps are not powerful enough to achieve the required pressure P_1. **Figures 11** and **12** plots the lift and drag forces measured for each operating

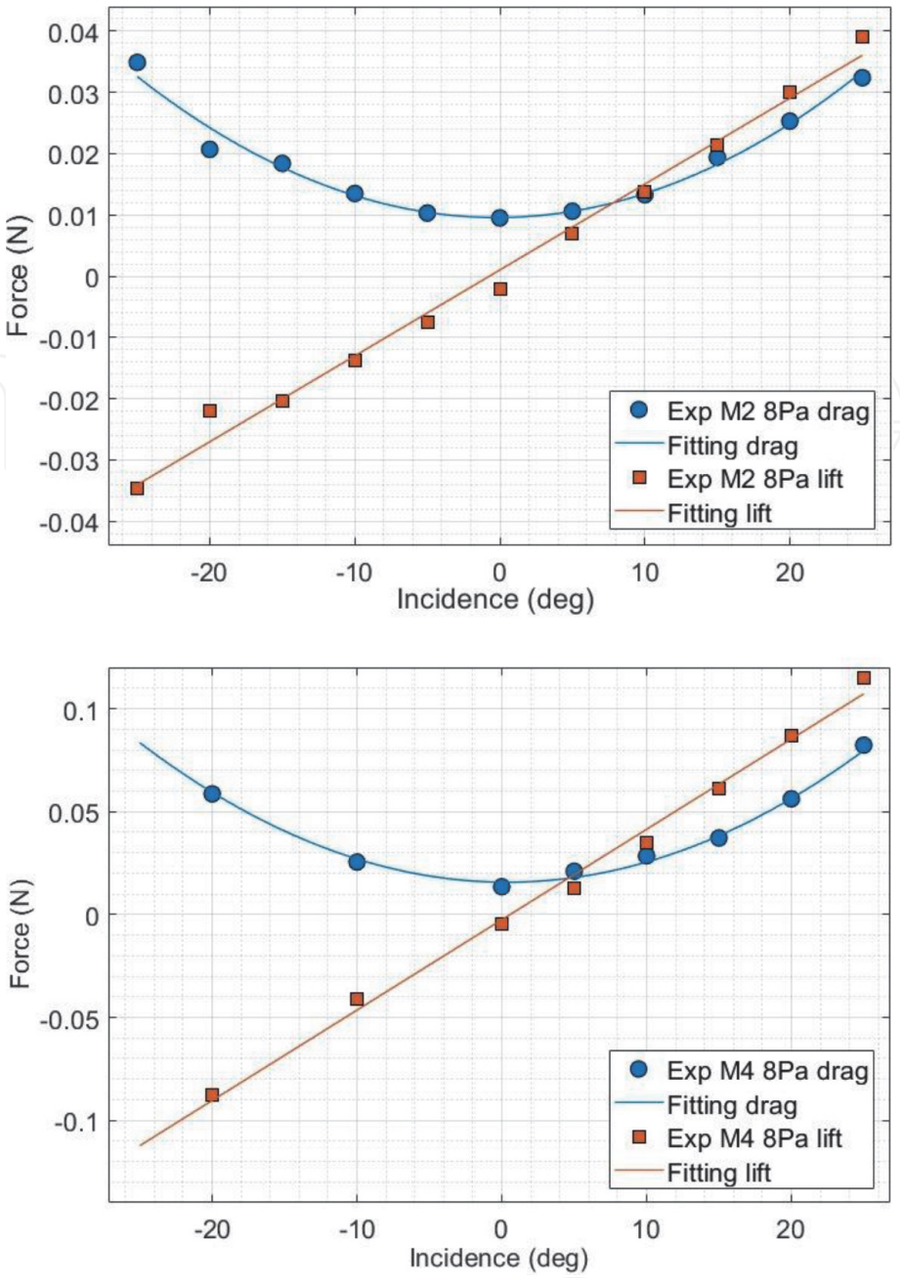

Figure 11.
Lift and drag forces: Mach 2–8 Pa and Mach 4–8 Pa.

condition. Whatever the experimental condition, the lift force behaves linearly with the angle of attack Θ, while the drag force follows a quadratic behavior at order 2. Lift forces can be described with an equation at first order as:

$$Lift = a\Theta - b \tag{3}$$

The fitting coefficients a and b are sumarized on **Table 6**.

Concerning the drag forces, an equation in second order can describe their evolution with the angle of attack, as follows:

$$Drag = c(\Theta)^2 + d\Theta + e \tag{4}$$

Table 7 presents the corresponding coefficients c,d and e.

The y-intercept is negative due to the shape of the waverider, the asymmetry between the two surfaces creates a negative lift at 0° angle of attack. Negative lift values means that the force acts in the same direction as the gravity force.

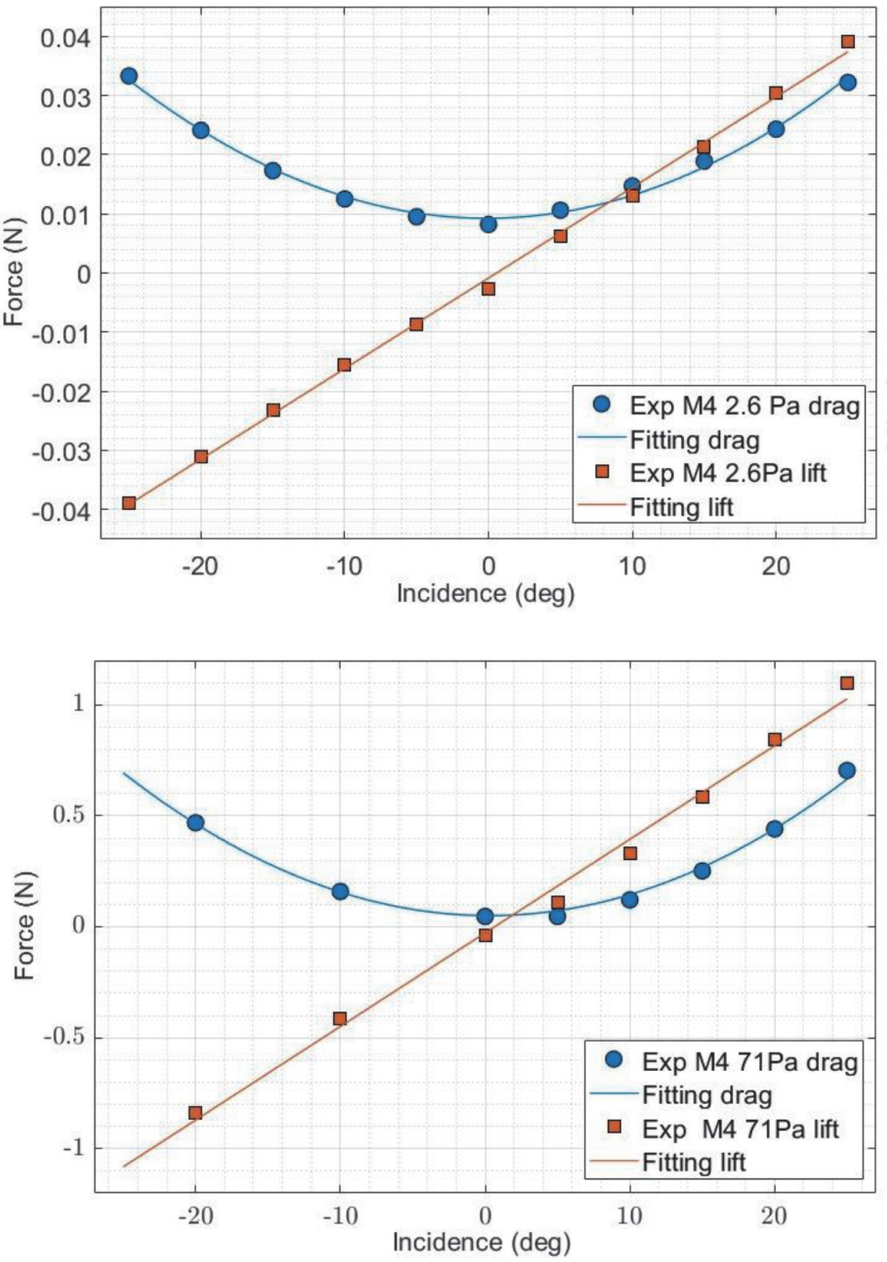

Figure 12.
Lift and drag forces: Mach 4–2 Pa and Mach 4–71 Pa.

Nozzle	a	b
Mach 2–8 Pa	$1.4.10^{-3}$	1.10^{-3}
Mach 4–2 Pa	$1.53.10^{-4}$	$8.63.10^{-4}$
Mach 4–8 Pa	$4.39.10^{-3}$	2.52^{-3}
Mach 4–71 Pa	$4.22.10^{-2}$	2.74^{-2}

Table 6.
Fitting coefficients for lift forces.

Comparisons of lift and drag forces show that those measured at the operating condition Mach 4–71 Pa are the highest and on the contrary, the lowest forces are obtained for Mach 2–8 Pa and Mach 4–2 Pa which are close in terms of values and shapes. One of the major parameters to design a space craft is the lift-to-drag ratio value. This value may determine the gliding ability of the waverider. The L/D ratio is a dimensionless number that can be determined directly from the aerodynamic

Nozzle	c	d	e
Mach 2–8 Pa	$3.74.10^{-5}$	$1.6.10^{-5}$	$9.56.10^{-3}$
Mach 4–2 Pa	$3.78.10^{-5}$	$1.02.10^{-5}$	$9.24.10^{-3}$
Mach 4–8 Pa	$1.05.10^{-5}$	7.53^{-5}	$1.57.10^{-3}$
Mach 4–71 Pa	1.10^{-5}	5.76^{-5}	$5.38.10^{-3}$

Table 7.
Fitting coefficients for drag forces.

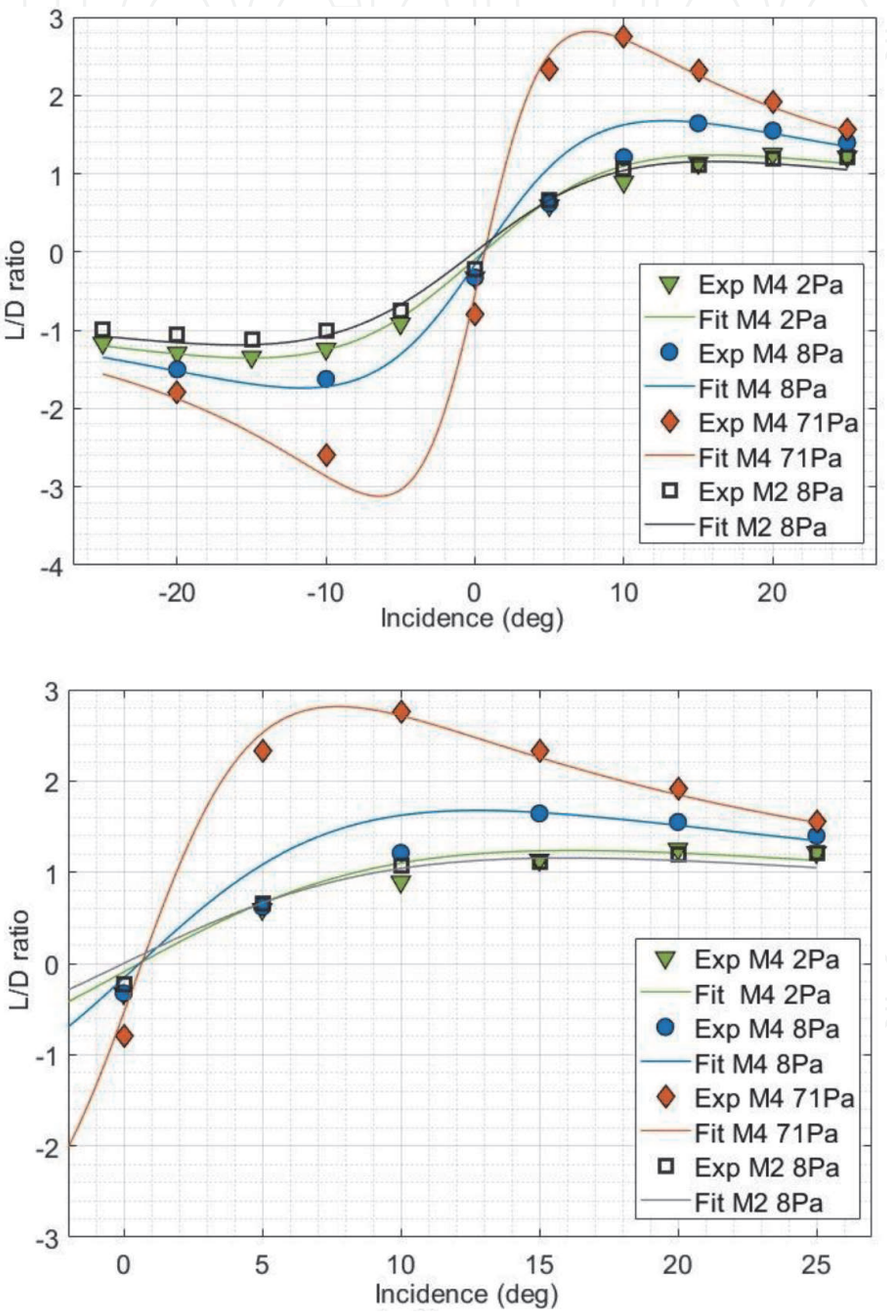

Figure 13.
Comparison of L/D ratio for all experimental conditions.

forces but also from the lift and drag coefficients. It does not follow a linear or quadratic function but has a more complex form. **Figure 13** presents the evolution of the ratio lift-to-drag with the angle of attack Θ for the overall experimental conditions. As can be seen, the L/D ratio will increase to reach a maximum and then

decrease and converge to 0.5–0.6. This evolution occurs for both positive and negative angles and presents a quasi symmetry around the 0° angle. This symmetry is possible because the thickness of the waverider is small, 6.6 mm, compared to its length, 100 mm, so that the waverider can be compared to a flat beveled plate. The waverider can be rotated 180° lengthwise and the sliding performance will be similar or even better if the fitting curves are realistic. Negative angle behavior shows that the optimal landing angle is between −5° and − 15°, depending on the ambient operating pressure of the nozzle used.

In the following, only the results of positive angles that illustrate the ability of the waverider to glide and maximize the travel distance before landing will be analyzed. The analysis of the results shows that the angle for which the value of the L/D ratio is maximum changes as a function of the operating conditions of the nozzle i.e. as a function of the static pressure P_1 and the Mach number. By relating the pressure P_1 of the flow to the atmospheric pressure for a given flight altitude, it is possible to associate to each nozzle an equivalent flight altitude, 80 km for Mach 4–2 Pa and Mach 2–8 Pa, 70 km for Mach 4–8 Pa and 50 km for Mach 4–71 Pa. This means that the angle of the maximum value of the L/D ratio decreases with altitude while the value itself increases. This is due to the fact that when the pressure decreases and the speed remains constant, the waverider must adapt its incidence in order to maintain an optimal L/D ratio and travel as far as possible. The influence of pressure in the isomach condition is shown in **Figure 14**. The values of the L/D ratio vary from 2.8 and 1.2 respectively for angles varying from 5° and 15°.

This observation shows that the waverider needs a high angle of attack at the beginning of its flight at high altitude, (low pressure) and must decrease its incidence to have an optimal L/D ratio when it decreases its flight attitude. A non-optimized L/D ratio will decrease the range of its flight. For example, if the waverider is launched at 80 km altitude with an incidence of 10° the L/D ratio is not optimal and for a flight altitude between 80 km and 50 km the waverider will be able to travel 33 km. Indeed between 80 km and 70 km, by referring to the curve for the Mach 2-8 Pa nozzle the value of L/D is of 0.89 and between 70 km and 50 km the M4 8Pa curve gives a L/D value of 1.21. However, by varying the angle of incidence the optimal L/D ratio between 70 km and 80 km is 1.25 and 1.64 for an

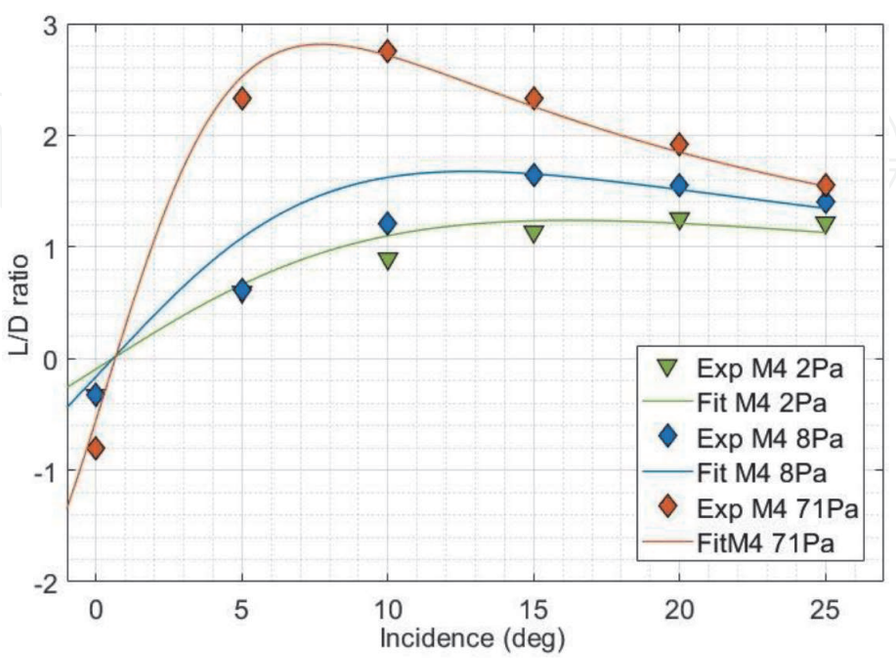

Figure 14.
Pressure influence on L/D ratio for isomach experimental conditions(Mach 4).

altitude ranged between 70 km and 50 km. With these data the new maximum flight distance that the waverider will be able to cover is 43 km. There is a variation of 10 km, which is not much, but during the last 50 km the L/D values could increase significantly due to the increase of the atmospheric pressure. The variation of the distance flown between the optimized and non-optimized flight can be greater, in the order of 50 km to 100 km. During the re-entry into the atmosphere, the speed of the waverider will vary and increase while decreasing the altitude. In this work, Mach 2 and Mach 4 nozzles operating with a static pressure of 8 Pa were used to observe the influence of the speed on the aerodynamic performance of the waverider. The L/D ratio is presented in **Figure 15**. As observed, the L/D ratio increases with Mach number as well as its optimal angle of attack to a lesser extent. For the Ma 2 8 Pa curve, the maximum is reached at about 25° while for the Ma 4 8 Pa curve the optimal angle is 15°. For the same pressure, when the speed increases, the value of the L/D ratio also increases. The maximum value of the L/D ratio can reach higher values for smaller angles, so to optimize the L/D ratio of waveriders, their speed must be increased when they fly at high altitude.

A first conclusion can be drawn from these experimental results. To optimize the performance of the waverider, the L/D ratio must be maintained at its optimal value by increasing the Mach number at high altitude and by increasing the angle of incidence by decreasing the flight altitude, in order to glide over the greatest possible distance. For the test model of this work the incidence will be between 20° and 25° at 80 km and will gradually decrease to 8° at 50 km. In terms of performance, the waverider will travel 1.2 km for every vertical kilometer lost at 80 km altitude and at 50 km, the waverider will travel more than 3 km. In fact, a waverider geometry is optimized for a specific flying speed and pressure. The geometry of this waverider is optimized to fligh at Mach 10 and altitudes ranging between 40 km and 50 km as Rolim presented in his paper, giving higest L/D values.

5.2 DSMC simulations and comparison with experimental results

Numerical simulations have been carried out using the direct Monte Carlo method, a stochastic method, solving the flow fields in transitional regime i.e. from continuum low density regime to free molecule regime. For this purpose, the

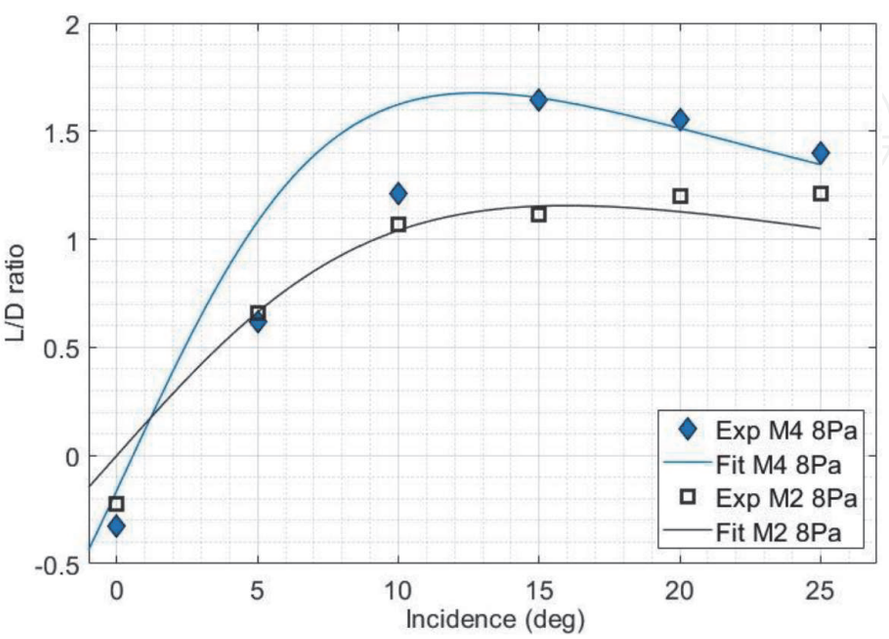

Figure 15.
Mach number influence on L/D ratio for isobar experimental conditions (P_1=8 Pa).

well-known DS3V software developed by Prof. Graeme A. Bird have been used [43, 44]. The main objective is to determine the accommodation parameters between the gaz flow and the waverider surface for our experimental conditions and analyze how they are related to rarefaction effects.

The comparison criterion between the numerical and experimental results are the drag and lift forces with the purpose to obtain numerical results as close as possible to those of the experiments.

We have selected the DS3V program by many reasons. The first one is the avaibility as it is free to download from the Bird website (http://www.gab.com.au). This program was designed to be able to run on personal computers with Microsoft windows. Finally, the use of DS3V is quite simple for a beginner as it uses a set of menus which creates files containing all the simulation information for post processing. However, one disadvantages associated with the DS3V codes is the creation/importation of the 3D geometry. Indeed, DS3V does not have an integrated geometry package and does not accept basic 3D CAD files. The geometry file have to be a Raw Triangle files with a series of x, y and z coordinates which form a 'triangle' and when put together they form a mesh.

To design the waverider, we have used the software Rhinoceros 7, because it can create triangular mesh with coordinates associated to each triangle apex. It is possible to select gas-surface interaction models among two models: the diffuse model or the CLL model [45–47]. The diffuse reflection model was adopted for this study. However, the reflection and absorption parameters characterizing the interaction with the waverider surface were adapted to the experimental conditions to be simulated. As the DSMC simulation is a probabilistic calculation, we considered that a flow time of 1 ms was sufficient to obtain valid results, and in particular this time is sufficient for the aerodynamic forces to be stabilized. Simulation were realized allowing 200 Mb memory. **Figure 16** shows the result obtained with the DS3V code

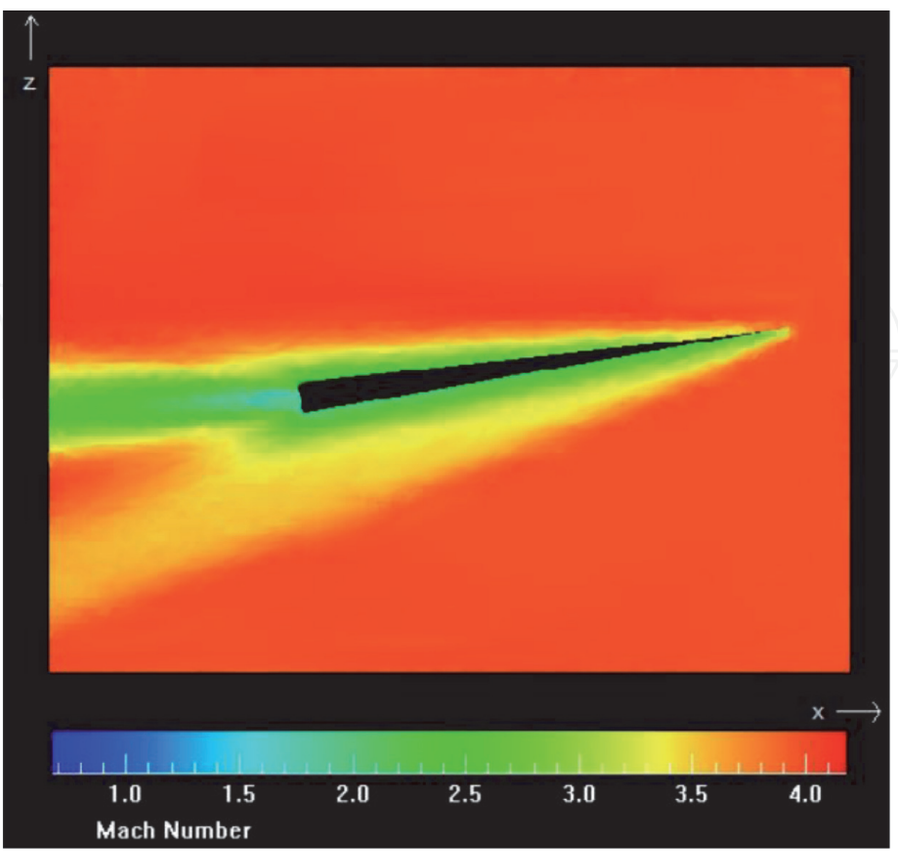

Figure 16.
Illustration of a numerical result obtained with DS3V for the experimental conditions Mach 4–8 Pa.

simulating the waverider with an incidence of 10° with conditions similar to those obtained experimentally with a Mach 4–8 Pa flow.

To achieve similarity between numerical and experimental curves, the accomodation coefficients which correspond to the specular reflection fraction and the absorbed fraction at surface are adapted. The sum of both fraction need to be equal to 1 for a consistent simulation. These coefficients are summarized in **Table 8** for each nozzle.

Parameter	Mach 2–8 Pa	Mach 4–2.66 Pa	Mach 4–8 Pa	Mach 4–71 Pa
Reflection	0.825	0.86	0.90	0.95
Absorption	0.175	0.14	0.10	0.05

Table 8.
Reflection and absorption accomodation parameters.

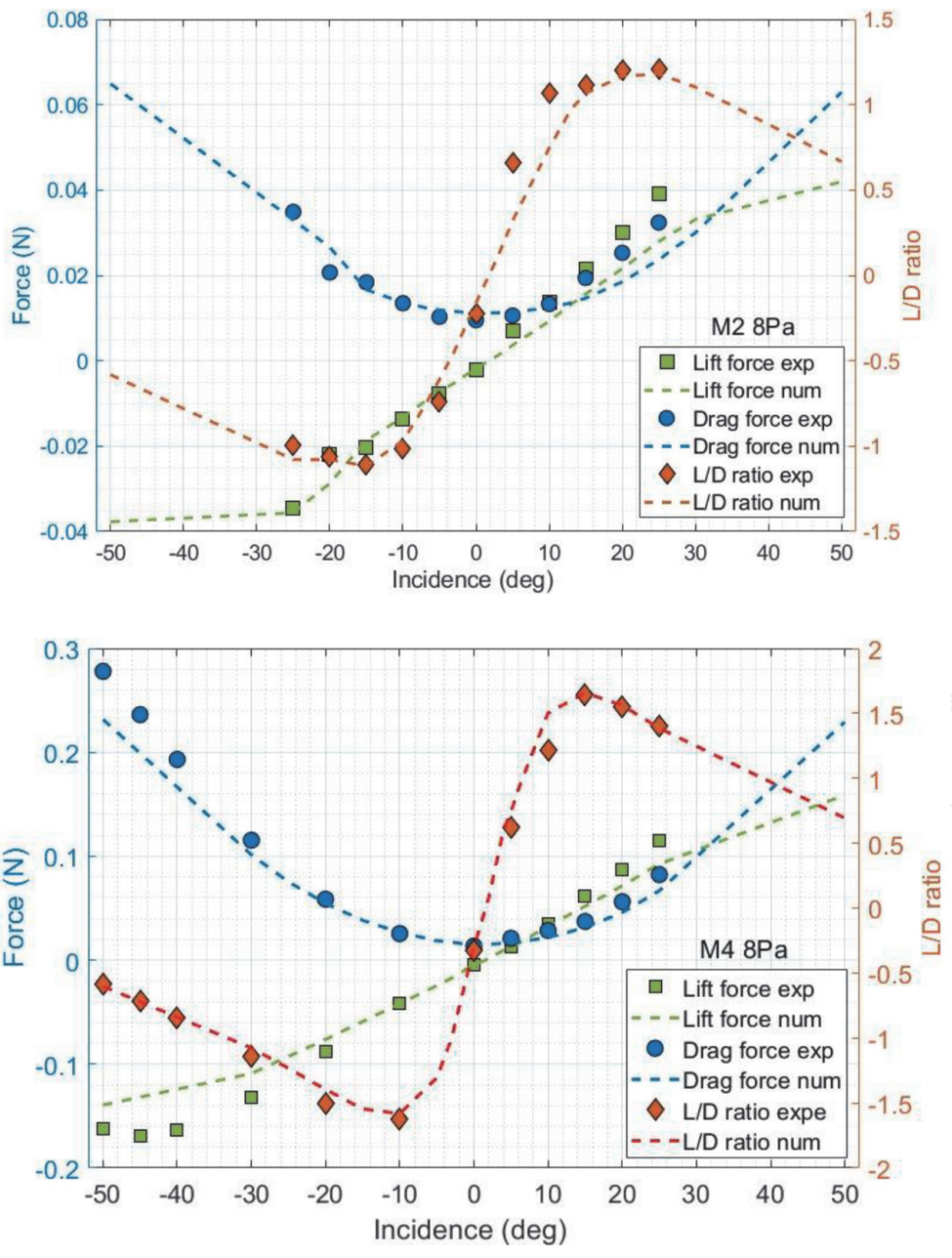

Figure 17.
Comparison of experimental and DS3V results for Mach 2–8 Pa and Mach 4–8 Pa.

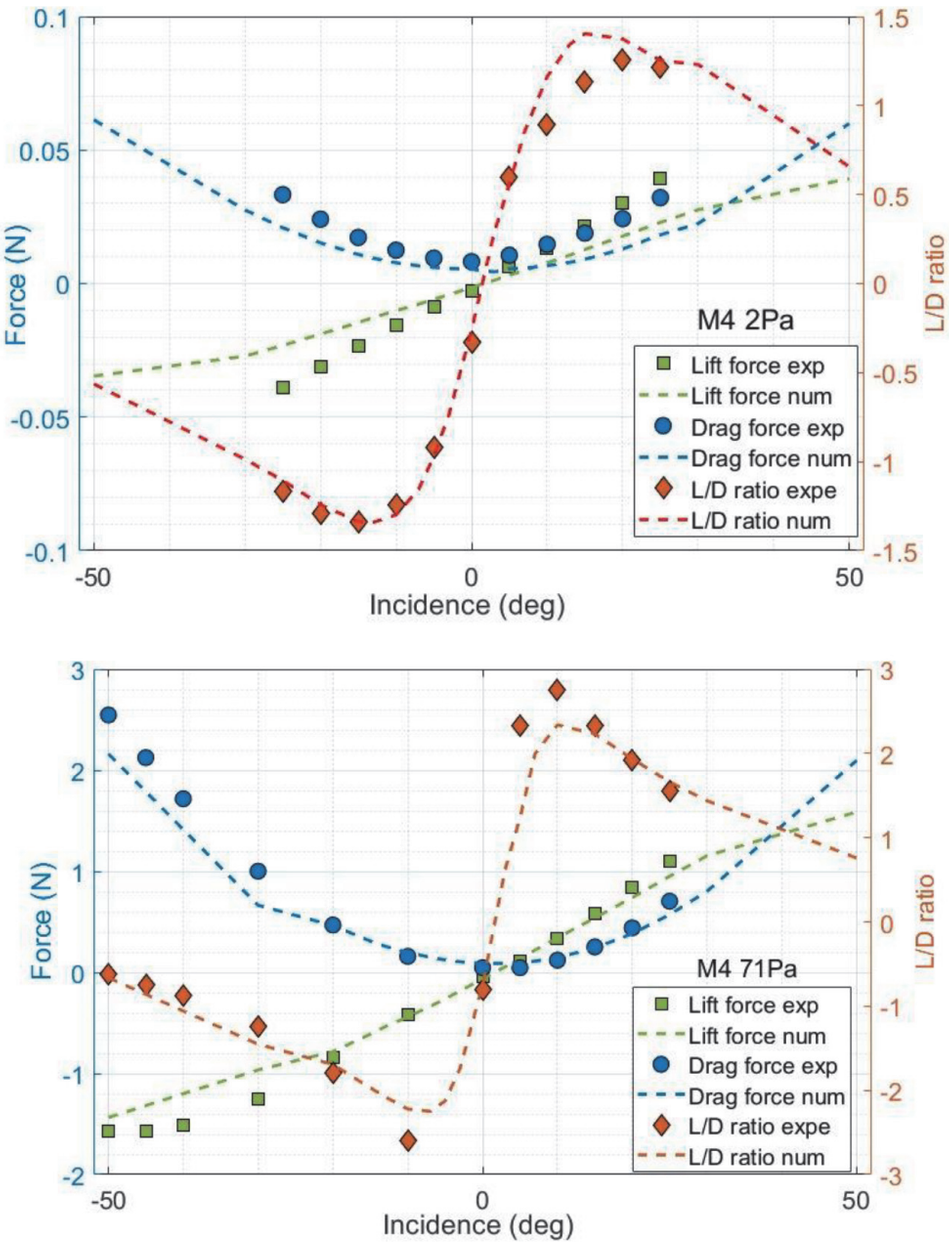

Figure 18.
Comparison of experimental and DS3V results for Mach 4–2.6 Pa and Mach 4–71 Pa.

For each of the experimental conditions i. e. nozles, the simulation of the flow around the wavereider was performed for the same incidences as those tested experimentally. Comparison between experimental and numerical results are presented on **Figures 17** and **18**. One can observe à good correlation between the numerical and the experimental results. Nevertheless, there are some differences in particular for the case Mach 2–8 Pa and Mach 4–2 Pa wich are the more rarefied conditions and presents small force values. The coefficient of the specular reflexion parameter seems to decrease with the rarefied parameter (Kn, $\psi = \frac{M}{\sqrt{Re}}$ or Re2). For low altitudes, typically the condition Mach 4–71 Pa, the reflection parameter tends to 1.

6. Discussion

6.1 Influence of rarefaction effects on fligth performance

The optimal flight conditions are given by the maximum values of the drag-lift ratio. These values will depend on the effects of rarefaction as summarized in

Table 9 in which are reported the maximum values of the ratio drag-lift, the angle of incidence corresponding for the various conditions of experiment studied in this work. Similarly, for each case, the values of the accommodation coefficient optimized in the framework of the DSMC numerical simulations are reported.

Figure 19 shows the maximum value of the L/D ratio and the corresponding angle as a function of the Knudsen number. It can be seen that the variation of the optimum angle of incidence increases linearly with the number of Knudsen, while the value of the L/D ratio decreases linearly with the logarithm of the number of Knudsen and this without distinction of the Mach number.

The study of the evolution of the ratio L/D with the rarefaction parameter, shows the influence of the Mach number as illustrated in **Figure 20**. Indeed, both the maximum value of the ratio L/D and the corresponding angle of incidence follow a linear variation for the experimental conditions at Mach 4, while the values for Mach 2 do not follow this trend. Isobar results shows that lower Mach number needs higher angle of incidence to optimize de ratio L/D.

As shown in **Figure 21**, the reflection accommodation coefficient used for the DSMC numerical simulations also follows a linear trend with the Knudsen number and increases towards 1 with decreasing Knudsen number. The same conclusions are made with the DSMC parameter (reflection parameter). However, when the comparison is made with the rarefaction parameter, only the results obtained with the same number of mach follow a linear trend.

In conclusion, for each parameter, the Knudsen number regroup all nozzles on a same trend (linear or logarithmic. It is not the case for the rarefaction parameter but a study isomach seems possible. To valid these conclusions, studies in hypersonic Mach 20 will be realized.

6.2 Estimation of the skin friction contribution

'The different effects of Mach number and geometry optimization on the aerodynamic performance of waveriders have been demonstrated. However, the effects of viscous drag, which have been little studied, can also have an impact on an elementary waverider geometry. For comparison purposes, and to complete our results, we consider the results presented by Rasmussen, carried out with a Mach number of 4 and with a geometry similar to the one used for the present study [48].

The ratio L/D can be expressed as:

$$L/D = \frac{L}{D_0 + D_f + D_b} \tag{5}$$

where L is the lift force, D_0 is the invicid wave drag, D_f is the friction drag and D_b is the base drag. In the following we assume that the base pressure is equal to the freestream pressure so that the base drag can be negleted [29]. The friction drag can be written as follows:

$$D_f = q S_w C_f \tag{6}$$

Parameter	Mach 2–8 Pa	Mach 4–2.66 Pa	Mach 4–8 Pa	Mach 4–71 Pa
angle of maximum L/D ratio	25	20	12.6	7.8
L/D ratio maximum	1.2086	1.2538	1.677	2.816
Reflection parameter	0.825	0.86	0.90	0.95

Table 9.
Reflection and absorption parameters.

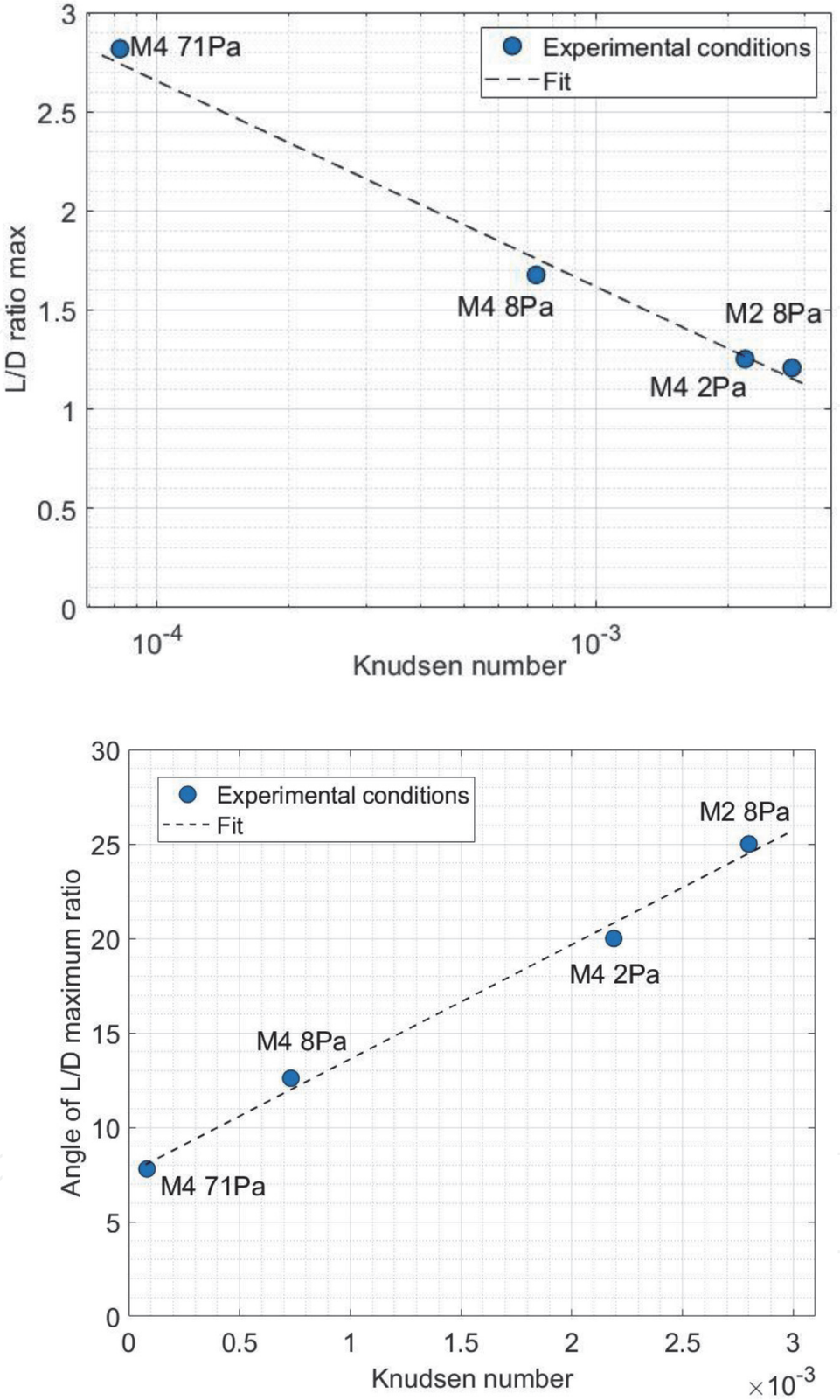

Figure 19.
Value of maximum L/D ratio and value of the corresponding angle of incidence as a function of the Knudsen number.

where q is the dynamic pressure, S_w is the wetted area of the waverider and C_f is the friction coefficient.

Friction effets are related to the development of the boundary layer, that can be influenced by many factors. The friction coefficient may depend of such factors as the Mach and Reynolds numbers, the wall temperature, and in continuum regime others physical properties such turbulence and flow

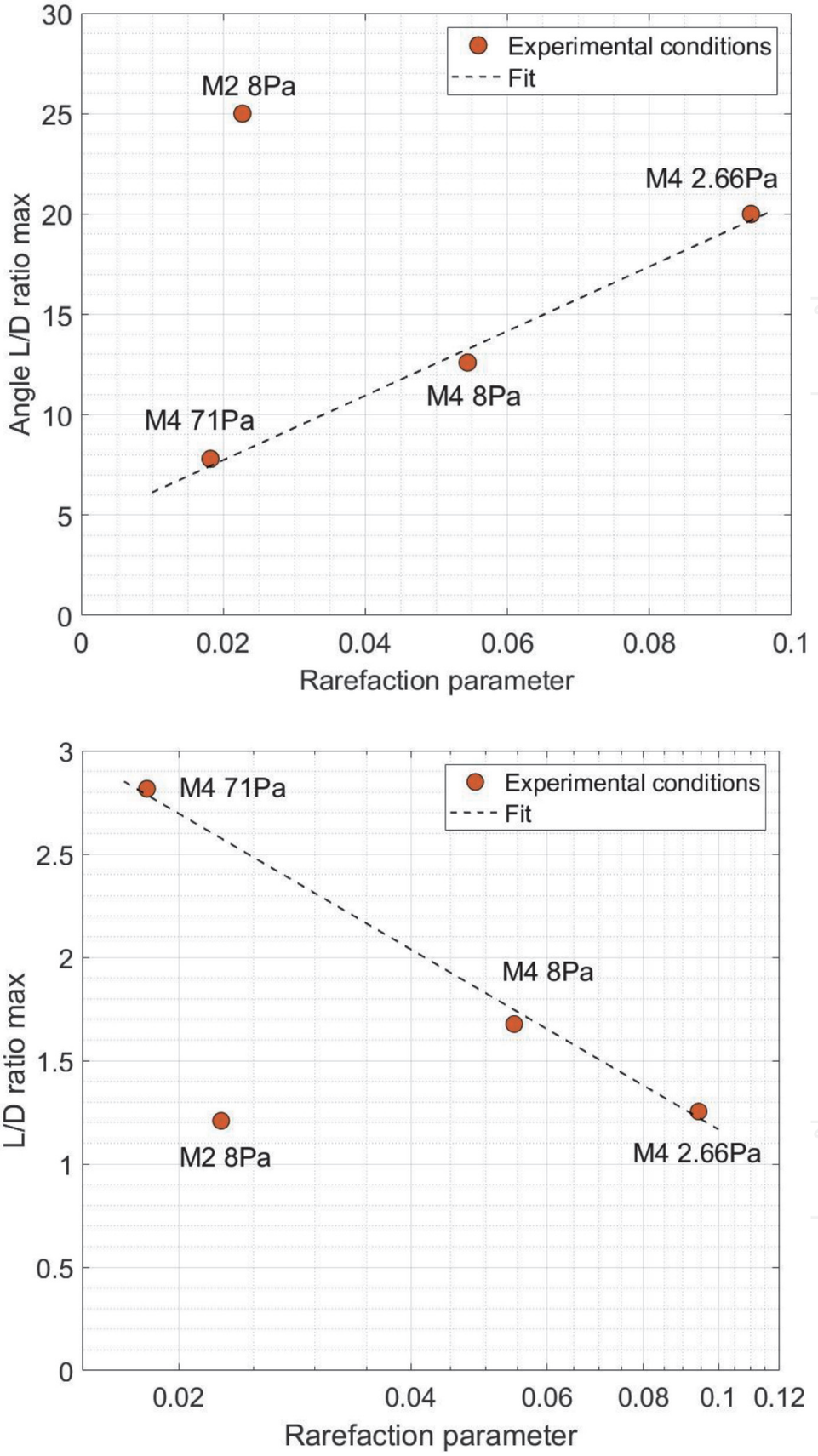

Figure 20.
Value of maximum L/D ratio and value of the corresponding angle of incidence as a function of rarefaction parameter value.

separation. This means that the definition of the friction coefficient can be a complex function that strongly depends on the flow properties and the objet model geometrie. For the current study, the waverider geometrie can be

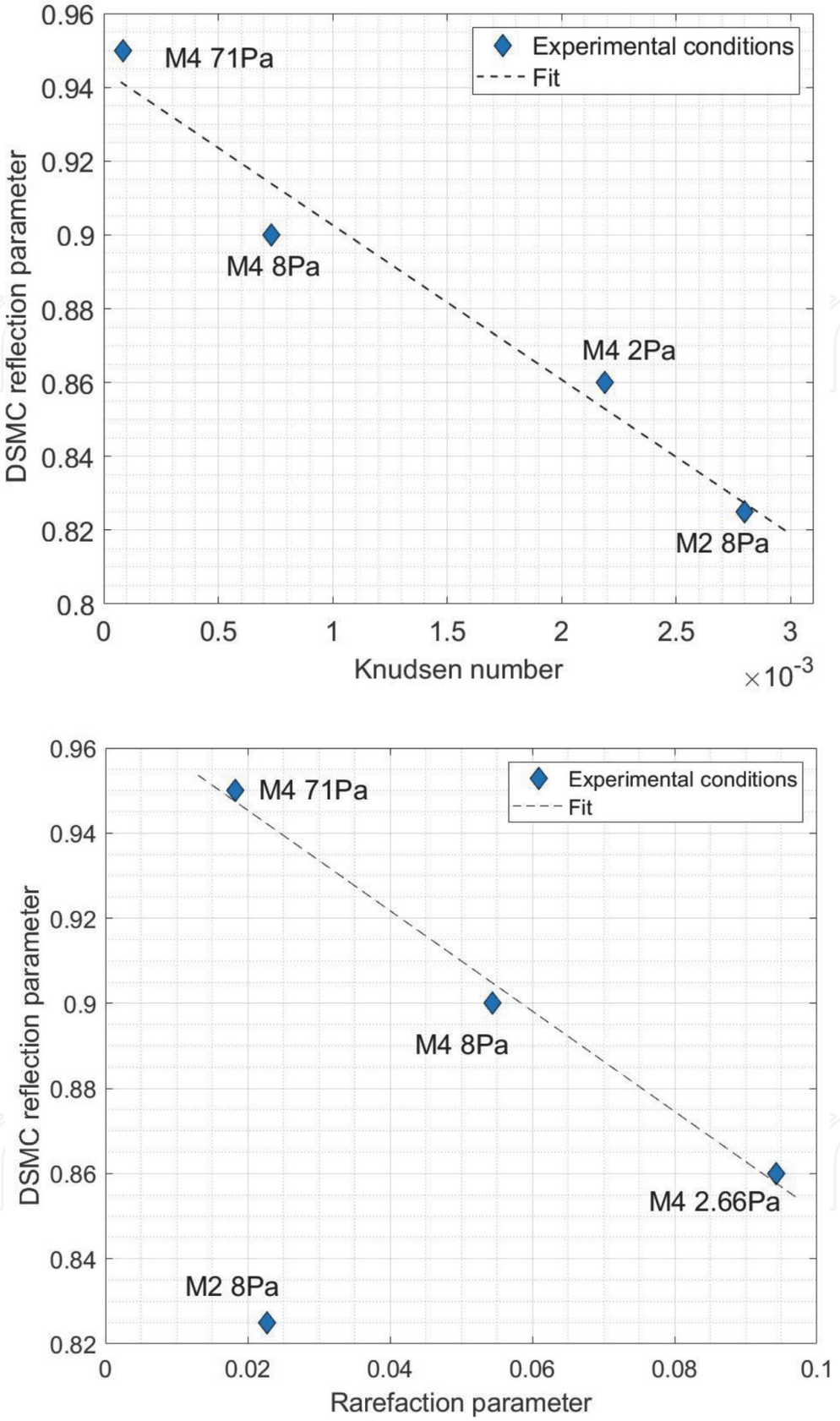

Figure 21.
Evolution of the DS3V reflection parameter as a function of the Knudsen number and the rarefaction parameter.

assimilated to a sharp plate, without the formation of a bow shock at the leading edge. Under this assumption, the skin friction can be defined by the following equation:

$$C_f = \frac{1.328 f(M, T_w/T_\infty, Re)}{\sqrt{\frac{\rho_\infty V_\infty l}{\mu_\infty}}} \tag{7}$$

Where $f(M, T_w/T_\infty, Re)$ is a function depending on Mach number, wall temperature and Reynolds number. For simplicity this function value can be assumed to be equal to 1 for $T_w/T_\infty = 1$, wich is our case. For the present study, the subscribe inf corresponds to the values of the free stream noted with the subscribe 1 in **Tables 1–4** presenting our experimental conditions.

Table 10 summarizes values of the friction coefficient for the experimental conditions presented by Rasmussen and those of the present experimental work as well as the maximum value of L/D ratio and the corresponding incidence angle of

Condition	C_f	$V^{2/3}/\text{Scos}\alpha$	Max (L/D ratio)
Mach 2–8 Pa	0.047	0.2074	1.2
Mach 4–2 Pa	0.030	0.2	1.25
Mach 4–8 Pa	0.0178	0.196	1.67
Mach 4–71 Pa	0.006	0.189	2.8
Rasmussen	0.001	0.12	8
Rasmussen	0.002	0.15	5.9
Rasmussen	0.003	0.175	4.2

Table 10.
Sumarize of the parameters for the optimum L/D ratio corresponding to the experimental conditions of this work and those predicted by Rasmussen.

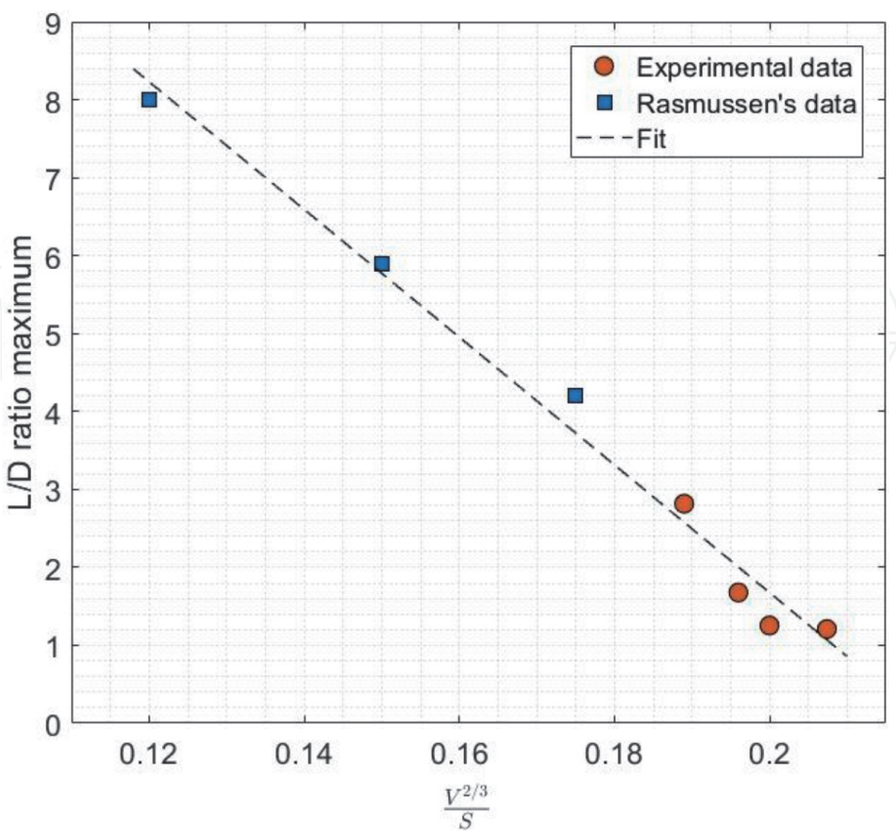

Figure 22.
Evolution of the maximum value of L/D as a function of the volume ratio.

the waverider. The value $V^{2/3}/(S\,cos\,\Theta)$, corresponds to the volume ratio wich is a function of the incidence angle Θ.

Figure 22 plots the Rasmussen data for the Mach 4 case and our experimental resuls which presents the linear evolution of the maximum L/D value with the

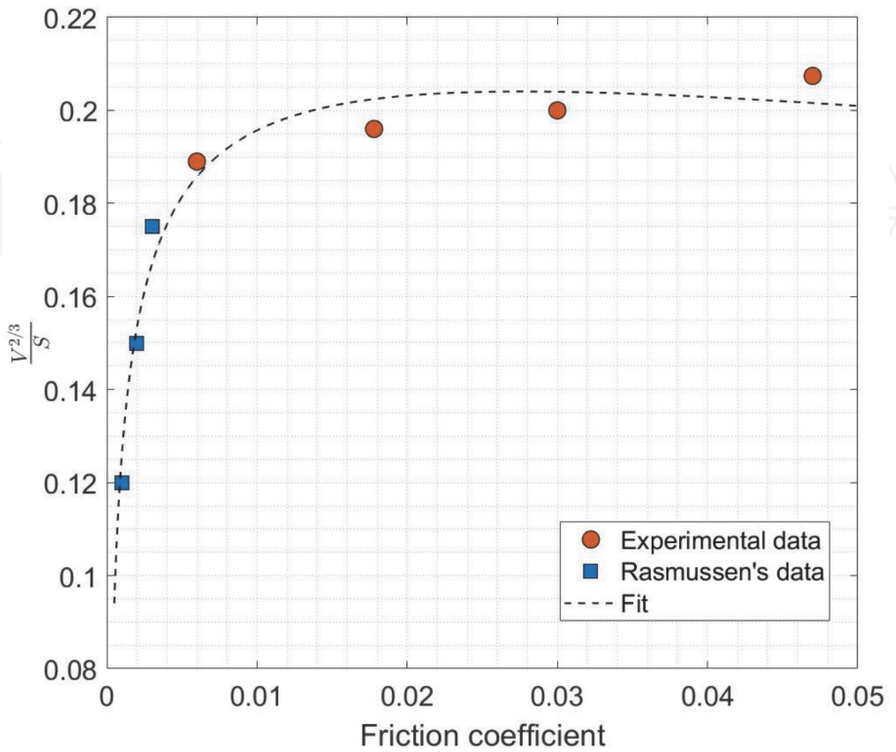

Figure 23.
Evolution of the volume angle as a function of the friction coefficient.

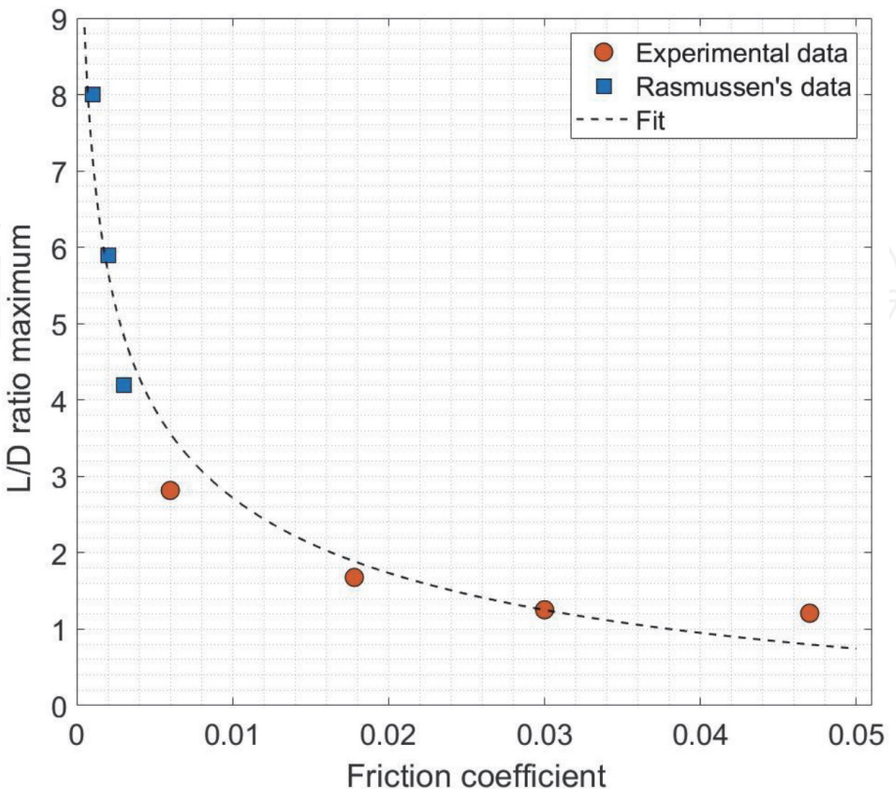

Figure 24.
Evolution of the maximum value of L/D as a function of the friction coefficient.

volume ratio. These results confirm the increase of the L/D maximum value as approaching continuous regime, the Rasmussen conditions presents lower friction coefficient values compared to those of our experimental conditions.

Moreover the evolution of the volume ratio with the friction coefficient presented on **Figure 23** seems to show that there is a limite value for volume ratio as rarefaction effects increases, showing that there is also a limite for the angle of attack to optimize the L/D ratio at high altitudes for a given geometrie. As presented in **Figure 24** the maximum L/D value decreases drastically with the increase of the friction coefficient which reflects the increase of the viscous effects.

7. Conclusions

This work focuses on the aerodynamic behavior of hypersonic gliders at high altitude. An experimental study of the behavior of a classic waverider has been conducted under supersonic and rarefied flow conditions for different values of the knudsen number. Measurements of drag and lift forces have been undertaken in the Marhy wind tunnel in supersonic operation for Mach 2 and Mach 4 numbers and equivalent pressures at altitudes between 5 km and 80 km. The experimental results showed that rarefaction effects produce a degradation of the flight performance of these waveriders, with a linear correlation between the value of the L/D ratio and the Knudsen number under the conditions studied. This is mainly due to the friction forces which increase with rarefaction due to viscous effects. This work also presents numerical simulation results obtained with the Bird DS3V code. The accomodation coefficients have been obtained with the CLL model for which the reflection and absorption coefficients have been adjusted according to the experimental conditions to be simulated. A linear correlation is also shown between these coefficients and the knudsen number. This study will be continued with an experimental study carried out in the marhy tunnel in hypersonic configuration at Mach 20 for an altitude of 100 km. First, the same waverider geometry will be studied, then a geometry will be optimized to improve the aerodynamic performances for more viscous flow conditions like those tested at Mach 20.

Acknowledgements

This work is fully financed by the Agence Nationale de la Recherche for the project APHYRA (APHYRA - 19-ASTR-0014-01)). PhD is supported by the French National Research Agency (ANR) as part of the Programme d'Investissement d'Avenir (LabEx CAPRYSSES; Grant No ANR-11-LABX-0006-01).

Conflict of interest

The authors declare that they have no conflict of interest.

Nomenclature

λ	Mean free path (m)
μ	Dynamic viscosity (Pa.s)
ρ	Density (kg.m^{-3})

Θ	Angle incidence of test model (Degres)
Cd	Drag coefficient
CL	Lift coefficient
C_f	Friction coefficient
D_0	Wave drag
D_f	Friction drag
D_b	Base drag
Kn	Knudsen number
L/D	Lift-to-drag ratio
Ma	Mach number
p	Pressure (Pa)
Re	Reynolds number
$Re\,2$	Reynolds number after choc
R_m	Specific gas constant = 287.058 $m^2.s^{-2}.K^{-1}$
S	Horizontal prejected area
T	Temperature (K)
U	Flow speed ($m.s^{-1}$)
V	Internal volume

Subscript

∞	Free-stream conditions
0	Stagnation conditions
w	Wall conditions

Author details

Noubel Hugo*† and Viviana Lago†
Laboratory ICARE-CNRS, Orléans, France

*Address all correspondence to: hugo.noubel@cnrs-orleans.fr

† These authors contributed equally.

References

[1] Ding, F., Liu, J., Shen, C. B., Liu, Z., Chen, S. H., & Fu, X. (2017). An overview of research on waverider design methodology. Acta Astronautica, 140, 190-205.

[2] Phoenix, A. A., Rogers, R. E., Maxwell, J. R., & Goodwin, G. B. (2018). Mach Five to Ten Morphing Waverider: Control Point Study. Journal of Aircraft, 1-12.

[3] Lewis, M. J., & McRonald, A. D. (1992). Design of hypersonic waveriders for aeroassisted interplanetary trajectories. Journal of Spacecraft and Rockets, 29(5), 653-660.

[4] Liu, W., Zhang, C. A., Han, H. Q., & Wang, F. M. (2016). Local piston theory with viscous correction and its application. AIAA Journal, 55(3), 942-954.

[5] Anderson, Jr, J. D. (2006). Hypersonic and high-temperature gas dynamics. American Institute of Aeronautics and Astronautics.

[6] Bowcutt, K. G., J. D. Anderson, and C. Diego. "Viscous optimized hypersonic waveriders. 1987." AIAA Paper: 87-0272.

[7] Rault, D. F. (1994). Aerodynamic characteristics of a hypersonic viscous optimized waverider at high altitudes. Journal of Spacecraft and Rockets, 31 (5), 719-727.

[8] Anderson, JR, John, Cang, J., & Mclaughlin, T. (1992, January). Hypersonic waveriders-Effects of chemically reacting flow and viscous interaction. In 30th Aerospace Sciences Meeting and Exhibit (p.302)

[9] Anderson, J. D., Lewis, M. J., Kothari, A. P., & Corda, S. (1991). Hypersonic waveriders for planetary atmospheres. Journal of Spacecraft and Rockets, 28(4), 401-410.

[10] Capriotti, D. (1987). Viscous optimized hypersonic waveriders. In 25th AIAA Aerospace Sciences Meeting (p. 272).

[11] Liu, W., Zhang, C. A., & Wang, F. M. (2018). Modification of hypersonic waveriders by vorticity-based boundary layer displacement thickness determination method. Aerospace Science and Technology, 75, 200-214.

[12] Rault, D., Willmoth, R., & Bird, G. (1991, June). An efficient DSMC algorithm applied to a delta wing. In 26th Thermophysics Conference (p. 1316).

[13] Kautz,F. A. II, , & Baron, J. (1991). Direct simulation of waveriders in hypersonic rarefied flow. In 26th Thermophysics Conference (p. 1317).

[14] Lewis, M. J., & Chauffour, M. L. (2005). Shock-based waverider design with pressure gradient corrections and computational simulations. Journal of aircraft, 42(5), 1350-1352.

[15] Lobbia, M. A., & Suzuki, K. (2014). Experimental investigation of a Mach 3.5 waverider designed using computational fluid dynamics. AIAA Journal, 53(6), 1590-1601.

[16] Nagashetty, K., Medhi, B., Sriram, R., Jagadeesh, G., & Reddy, K. P. J. (2017). Tomographic Visualization of the Hypersonic Flow Field over a Waverider. In 30th International Symposium on Shock Waves 2 (pp. 1437-1440). Springer, Cham.

[17] Rolim, Tiago Cavalcanti, et al. "Experimental results of a Mach 10 conical-flow derived waverider to 14-X hypersonic aerospace vehicle." Journal of Aerospace Technology and Management 3 (2011): 127-136.

[18] Rolim, T. C., Toro, P. G. D. P., Minucci, M. A. S., Oliveira, A. D. C. D.,

& Follador, R. D. C. (2011). Experimental results of a Mach 10 conical-flow derived waverider to 14-X hypersonic aerospace vehicle. Journal of Aerospace Technology and Management, 3(2), 127-136.

[19] Galloway, E. M., Gilmore, M., Jeffery, R., & Harvey, J. (1991). Heat transfer to a delta wing and two waverider wings in rarefied hypersonic flow. Rarefied gas dynamics, 505-513.

[20] Macrossan, M. N. (2006, July). Scaling parameters for hypersonic flow: correlation of sphere drag data. In Twenty-fifth Int. Symp. Rarefied Gas Dynamics, St. Petersburg, Russia (pp. 759-764).

[21] Orlik, E., Fedioun, I., & Davidenko, D. (2011). Boundary-layer transition on a hypersonic forebody: experiments and calculations. Journal of Spacecraft and Rockets, 48(4), 545-555.

[22] Fedioun, I., & Orlik, E. (2012). Boundary layer transition on the LEA hypersonic vehicle forebody. In 18th AIAA/3AF Int. Space Planes & Hypersonic Systems & Technol. Conf. (p. 5864).

[23] Rodi, P., & Bennett, G. (2012, June). High lift-to-drag ratio waveriders for missions in the Martian atmosphere. In 30th AIAA Applied Aerodynamics Conference (p. 3221).

[24] Knittel, J. (2015). Aero-Assisted Spacecraft Missions Using Hypersonic Waverider Aeroshells (Doctoral dissertation).

[25] Lunan, Duncan A. "Waverider, a revised chronology." 20th AIAA International Space Planes and Hypersonic Systems and Technologies Conference. 2015.

[26] Nonweiler, T. R. F. "Aerodynamic problems of manned space vehicles." The Aeronautical Journal 63.585 (1959): 521-528.

[27] Rasmussen, Maurice L. "Waverider configurations derived from inclined circular and elliptic cones. "Journal of Spacecraft and Rockets 17.6 (1980): 537-545.

[28] Ding, Feng, et al. "An overview of research on waverider design methodology." Acta Astronautica 140 (2017): 190-205.

[29] Anderson, JR, J., Frederick Ferguson, and MARK LEWIS. "Hypersonic waveriders for high altitude applications." 29th Aerospace Sciences Meeting. 1991.

[30] Townend, L. H. "Research and design for lifting reentry." Progress in Aerospace Sciences 19 (1979): 1-80.

[31] Rolim, T. C. (2009). Experimental analyisis of a hypersonic waverider (Doctoral dissertation, Instituto Tecnológico de Aeronáutica).

[32] Boutemedjet, Abdelwahid, et al. "Wind tunnel measurement of small values of rolling moment using six-component strain gauge balance." Measurement 116 (2018): 438-450.

[33] Reis, M. L. C. C., R. M. Castro, and O. A. F. Mello. "Calibration uncertainty estimation of a strain-gage external balance." Measurement 46.1 (2013): 24-33.

[34] Aroesty, Jerome. Sphere drag in a low density supersonic flow. California Univ. Berkley Inst. of Engineering Research, 1962.

[35] Hoffmann, Karl. An introduction to measurements using strain gages. No. BOOK. Darmstadt: Hottinger Baldwin Messtechnik, 1989.

[36] Higson, GRt. "Recent advances in strain gauges." Journal of Scientific Instruments 41.7 (1964): 405.

[37] Tufte, O. N., and D. Long. "Recent developments in semiconductor

piezoresistive devices." Solid-state electronics 6.4 (1963): 323-338.

[38] Schlegat, Thomas, and Klaus Hannemann. "Experimental Investigation of Rarefaction Effects on Aerodynamic Coefficients of Slender and Blunt Re-entry Vehicles." International Conference on High-Speed Vehicle Science and Technology 2018 (HiSST). 2018.

[39] Coumar, Sandra. Study of physical mechanisms induced by a plasma actuator for super/hypersonic rarefied flows applied to atmospheric entries. Diss. Université d'Orléans, 2017.

[40] Boyd, Iain D. "Predicting breakdown of the continuum equations under rarefied flow conditions." AIP Conference Proceedings. Vol. 663. No. 1. American Institute of Physics, 2003.

[41] Riabov, Vladimir V. "Comparative similarity analysis of hypersonic rarefied gas flows near simple-shape bodies." Journal of Spacecraft and Rockets 35.4 (1998): 424-433.

[42] Probstein, Ronald F., and Nelson H. Kemp. "Viscous aerodynamic characteristics in hypersonic rarefied gas flow." Journal of the Aerospace Sciences 27.3 (1960): 174-192.

[43] Bird, G. A. "Molecular gas dynamics and direct simulation Monte Carlo." Clarendon Press Oxford Science (1998).

[44] Bird, G. A., and D. S. M. C. Visual. "Program for Three-Dimensional Flows." The DS3V Program User's Guide, Version 2 (2006).

[45] Zuppardi, Gennaro, and Giuseppe Mongelluzzo. "Computer analysis of rarefied aerodynamics around a winged space-plane for Mars entry." Advances in Aircraft and Spacecraft Science 8.2 (2021): 169.

[46] Zuppardi, Gennaro. "Influence of partial accommodation coefficients on the aerodynamic parameters of an airfoil in hypersonic, rarefied flow." Advances in aircraft and spacecraft science 2.4 (2015): 427.

[47] Hedahl, Marc O., and Richard G. Wilmoth. Comparisons of the Maxwell and CLL gas/surface interaction models using DSMC. National Aeronautics and Space Administration, Langley Research Center, 1995.

[48] Rasmussen, M. "Viscous effects on the performance of cone-derived waveriders." 10th Atmospheric Flight Mechanics Conference. 1983.